Journal Pre-proofs

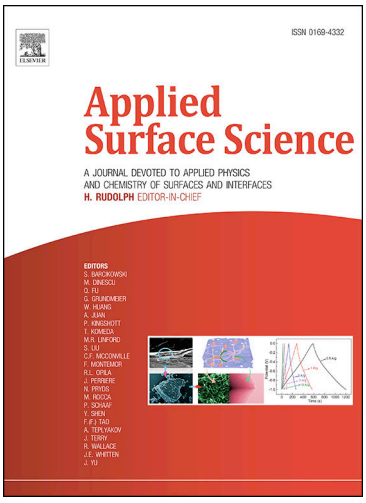

Formation of Mo_2C/hollow tubular g-C_3N_4 hybrids with favorable charge transfer channels for excellent visible-light-photocatalytic performance

Chen Zhang, Yin Zhou, Wenjun Wang, Yang Yang, Chengyun Zhou, Longlu Wang, Lei Lei, Donghui He, Hanzhuo Luo, Danlian Huang

PII: S0169-4332(20)31514-2
DOI: https://doi.org/10.1016/j.apsusc.2020.146757
Reference: APSUSC 146757

To appear in: *Applied Surface Science*

Received Date: 8 March 2020
Revised Date: 11 May 2020
Accepted Date: 21 May 2020

Please cite this article as: C. Zhang, Y. Zhou, W. Wang, Y. Yang, C. Zhou, L. Wang, L. Lei, D. He, H. Luo, D. Huang, Formation of Mo_2C/hollow tubular g-C_3N_4 hybrids with favorable charge transfer channels for excellent visible-light-photocatalytic performance, *Applied Surface Science* (2020), doi: https://doi.org/10.1016/j.apsusc.2020.146757

This is a PDF file of an article that has undergone enhancements after acceptance, such as the addition of a cover page and metadata, and formatting for readability, but it is not yet the definitive version of record. This version will undergo additional copyediting, typesetting and review before it is published in its final form, but we are providing this version to give early visibility of the article. Please note that, during the production process, errors may be discovered which could affect the content, and all legal disclaimers that apply to the journal pertain.

© 2020 Published by Elsevier B.V.

Journal Pre-proofs

Formation of Mo_2C/hollow tubular g-C_3N_4 hybrids with favorable charge transfer channels for excellent visible-light-photocatalytic performance

Chen Zhang [a,b*], Yin Zhou [a,b], Wenjun Wang [a,b], Yang Yang [a,b], Chengyun Zhou [a,b], Longlu Wang [c], Lei Lei [a,b], Donghui He [a,b], Hanzhuo Luo [a,b], Danlian Huang [a,b *]

[a] College of Environmental Science and Engineering, Hunan University, Changsha, 410082, PR China

[b] Key Laboratory of Environmental Biology and Pollution Control, Hunan University, Ministry of Education, Changsha 410082, PR China

[c] College of Electronic and Optical Engineering & College of Microelectronics, Nanjing University of Posts and Telecommunications, Nanjing 210023, P. R. China.

[*] Corresponding author at: College of Environmental Science and Engineering, Hunan University, Changsha, Hunan 410082, China. E-mail address: zhangchen@hnu.edu.cn (C. Zhang); huangdanlian@hnu.edu.cn (D.L. Huang)

Journal Pre-proofs

Abstract: The pharmaceutical products have becoming ubiquitous in aquatic environment. Photocatalytic degradation is considered as a promising strategy to address this environmental threat. Here we showed new Mo_2C/hollow tubular g-C_3N_4 hybrids (Mo_2C/TCN) consisting of well-designed direct Z-scheme heterojunction with favorable charge transfer channels for efficient contaminants degradation. Compare to the traditional Mo_2C/g-C_3N_4 type-I heterojunction reported in the previous literature, the powerful direct Z-scheme heterojunction retains the original redox ability of the component without changing its oxidation and reduction potential. By virtue of the hollow tubular architecture, more incident electrons are expected to be rapid trapped by Mo_2C nanoparticles, which contributes to the effective separation of photoinduced hole-electron pairs. As a result, the optimized Z-scheme system exhibits impressive visible-light photocatalytic performance. Especially, the 2 wt% Mo_2C/TCN photocatalysts exhibits superior photocatalytic performance for tetracycline degradation with a reaction rate of 0.0391 min^{-1}, which is 3-times and 9-times higher than those of TCN and pristine g-C_3N_4, respectively. The outstanding performance strongly depends on the synergistic effects among the favorable electrical conductivity of Mo_2C and the multitude of charge transfer channels provided by the Z-scheme heterojunction. This work provides a new idea of designing direct Z-scheme material and it sheds novel insight to establish photocatalytic model for environmental amendment.

Key words: g-C_3N_4; Photocatalytic; Z-scheme heterojunction; Degradation

Journal Pre-proofs

1. Introduction

Antibiotic contamination has raised world-wide concerns due to its threats to the organisms in ecosystem and indefinite environmental impacts [1]. Numerous studies were conducted for removing the contaminants in wastewater, including physical adsorption, chemical technology, and biological degradation [1-5]. The photocatalytic technology has become a promising environmental pollution treatment technology and made a series of achievements. Photocatalytic degradation of antibiotics from wastewater has aroused tremendous interests due to its high efficiency [6]. After the discovery of photocatalytic properties in TiO_2 [7], semiconductor based photocatalysis has been an area of intense research for last 50 years. TiO_2 represents an effective photocatalyst due to its relatively high reactivity and chemical stability [8]. However, the wide band gap of TiO_2 limits its applications, since it can only absorb light below wavelengths of 400 nm. To solve this problem, a group of visible light photocatalysts have been investigated. For example, metal oxides (e.g., Fe_2O_3, WO_3 and $BiVO_4$) [9], transition metal phosphides (e.g., Ni_2P, FeP and CoP) [10], metal sulfides (CdS) [11], nitrides and oxynitrides (Ta_3N_5 and TaON) [12]. Over the past decade, new photocatalyst materials have been designed and fabricated one after another, including graphic carbon nitride (g-C_3N_4) [13], metal organic frameworks (MOFs) [14] and polyoxometalates [15]. Many of the most recent developments in visible-light-photocatalysis have been realized by utilizing the nano-assembly systems or controlling the morphology of nanomaterials, including construction of heterojunctions, doping

elements such as C, N, S to modulate the energy band, addition of quantum dots or dyes for better light sensitization, and adjusting the structure and morphology of nanomaterials [16]. Whereas, several crucial challenges are still being faced, such as rapid recombination of photo-induced charge carriers, low reusability due to photocorrosion, and deficient reactive sites [17]. Developing new and efficient photocatalysts is the focus of this technology [18-21].

As an innovative material, graphic carbon nitride (g-C_3N_4) attracted great attention from researchers among the numerous photocatalysts due to its suitable band gap of 2.7 eV and desirable visible-light response [22]. However, the catalytic efficiency of g-C_3N_4 is not satisfactory because of the high recombination of photo-generated charge carriers[23]. Hence, different strategies have been developed to address these intrinsic drawbacks, such as morphological engineering, heterojunction construction, heteroatoms doping, et al. Morphological engineering has always been a vital research direction to boost the catalytic performance of g-C_3N_4 [24, 25]. Based on different synthesis methods, the obtained g-C_3N_4 expressed different dimensional morphologies (zero-dimensional (0D) quantum dots [26], 1D nanorods/nanotubes [27], 2D nanosheets [28-30] , 3D (hollow) microspheres [31]) with superior photoelectrical properties and catalytic performance. In particular, the 1D g-C_3N_4 nanorods/nanotubes can enrich active sites in the radial direction and allow the electron swiftly transfer along the specific direction, thus realizing effectively spatial charge separation [32]. The synthetic methods of the above-mentioned g-C_3N_4 nanotubes are mainly confined to liquid-phase reactions, template-assisted processes and wet-chemical routes, which

are not intrinsically controllable [33]. Our group has reported a facile method to synthesize hollow tubular g-C_3N_4 for disinfection and tetracycline (TC) degradation [34]. This cavity structure endows g-C_3N_4 with favourable efficiencies of mass transfer, high specific surface area and optimizes the utilization of photons.

Mxenes, as a novel member of 2D materials, have stimulated growing concerns recently. Among them, molybdenum carbide (Mo_2C) has attracted intensive research interest for its unique electronic structures and catalytic activities [35-38]. Compared with the transition metal sulfides, such as MoS_2 [39] and WS_2 [40], Mo_2C is more earth-abundant and displays excellent physicochemical properties, benefiting for the charge separation in photocatalysis. The study of Mo_2C is almost focused on electrocatalysis field while the instances for the utilization of Mo_2C in the treatment of antibiotics is absent, mostly due to the rapid recombination of photo-induced charge carriers. Song et al. [41] firstly reported the Mo_2C@C/2D g-C_3N_4 heterostructure for hydrogen production in 2018. Then, several researchers investigated the Mo_2C/g-C_3N_4 hybrids for their excellent photocatalytic performance [42-44]. Unfortunately, the Mo_2C/g-C_3N_4 heterojunctions reported previously are mainly conventional type-I or type-II heterojunction. For conventional type-I or type-II heterojunction, a dilemma is the lack of good compatibility between the efficient separation of electron/hole (e^-/h^+) pairs and strong redox ability. The advantages of conventional type-I or type-II heterojunction are at the expense of redox ability of charge carriers, which suggest a weakened driving force that may fail to drive a specific photocatalytic reaction and restrict the application of photocatalysts. In contrast to the above heterojunction, direct Z-scheme

photocatalysts have been paid great attention [45]. The redox ability of direct Z-scheme heterojunction photocatalyst can be optimized and the migration of photogenerated electrons between two semiconductors is favorable due to the electrostatic attraction. Direct Z-scheme photocatalysts preserves sufficient energy levels of e^-/h^+ and maintains higher oxidation and reduction potentials for the further redox reactions. However, to the best of our knowledge, Mo_2C/g-C_3N_4 direct Z-scheme heterojunction has not been reported.

In this work, we reported Mo_2C decorated tubular like g-C_3N_4 (Mo_2C/TCN) to construct Z-scheme heterostructure photocatalytic system for highly active and stable photocatalytic degradation of water contaminants. Mo_2C/TCN as an optimized Z-scheme system maintains high oxidation and reduction abilities and the migration of photo-induced charge carriers is more favorable. Such well-matched heterostructure was constructed by rational choice semiconductor with optimized bandgap structure. The TCN with narrowed bandgap of 2.43 eV due to the formation of tubular like morphology and the variation of precursors [46]. The apparent difference in band gap energies of Mo_2C and TCN offers great potential for constructing Z-scheme heterostructure. We further presented photoelectron spectroscopy evidence for the formation of Mo_2C/TCN direct Z-scheme system. X-ray photoelectron spectroscopy (XPS) confirmed that the electrons were transferred from TCN to Mo_2C in the Mo_2C/TCN photocatalytic system and eliminated the possibility of type-II heterojunction. The introduction of Mo_2C improves the efficiency for photon utilization, provides trapping sites for photo-induced electrons and facilitates the separation of

electron-hole pair, thus prolonging charge carriers' lifetime. The specific 1D hollow tubular structure provides favorable channel for electrons transport. This unique photocatalytic system provides a new insight for the environmental protection and it is anticipated that this highly efficient direct Z-scheme photocatalysts can be a promising candidate for other reaction system.

2. Experimental Section

2.1 Reagents

Melamine ($C_3N_3(NH_2)_3$), urea ($CO(NH_2)_2$), ammonium heptamolybdate tetrahydrate ($(NH_4)_6Mo_7O_{24}\cdot 4H_2O$), hydrochloric acid (HCl), aniline (C_6H_7N), poly(vinyl alcohol) (PVA), disodium oxalate ($Na_2C_2O_4$), 2,2,6,6-tetramethylpiperidine-1-oxyl (TEMPOL), $C_4H_{10}O$ (TBA) and TC were purchased from Sinopharm Corporation Ltd. (Shanghai, China). In this research, all reagents used were of analytical grade, without further purification.

2.2 Synthesis of catalysts

2.2.1 Synthesis of Mo_2C catalyst

The synthesis of Mo_2C was based on the published method, with slight modification [47]. Typically, $(NH_4)_6Mo_7O_{24}\cdot 4H_2O$ (2.0 mmol) and aniline (36.0 mmol) were first added to 40 mL deionized (DI) water. Then, under magnetic stirring, HCl aqueous solution (1.0 M) was dropwise added until white precipitate appeared. After reaction in an oil bath (50 °C) for 4 h, the white precipitate was suction filtered and

Journal Pre-proofs

washed three times with DI water and ethanol. The filtered product was dried overnight at 60 °C, and then, a white powder was obtained. Next, these synthesized powders were transferred into a tube furnace and heated from ambient temperature to 775 °C at a ramp rate of 2 °C min^{-1} and maintained for 3 hours. The furnace was filled with N_2 gas. After naturally cooling to room temperature, the black Mo_2C sample formed.

2.2.2 Synthesis of tubular g-C_3N_4 photocatalyst

A yellow bulk g-C_3N_4 (CN) sample was prepared via calcination of melamine at muffle furnace for 4 h. The reaction conditions were 550 ℃ with a ramp rate of 2.3 ℃ min^{-1}. The tubular g-C_3N_4 (TCN) was synthesized according to a method published by our group with little modification [34]. We first conducted a hydrothermal process: 8 g melamine and 6.42 g urea were transfer into a Teflon-lined stainless-steel autoclave with 70 ml DI water solution and kept at 180 ℃ for 24 h. The precipitate was collected by filter and washed with DI water and ethanol for three times. After dried in an oven, the white powder was calcinated at 550 ℃ for 4 h at a rate of 2.3 ℃ min^{-1}. After naturally cooling to room temperature, TCN obtained.

2.2.3 Preparation of Mo_2C/TCN photocatalysts

The Mo_2C/TCN photocatalysts were synthesized by ultrasonic-assisting deposition method [48]. A certain amount of Mo_2C and TCN was dispersed in 25 mL methanol. The dispersion was ultrasonicated for 1h at room temperature under the frequency of 40 kHz, power of 240 W, and then stirred until methanol was completely volatilized. The yellowish powder was obtained after drying overnight in an oven at 60 ℃. According to this method, the Mo_2C/TCN photocatalysts with different mass ratios

of Mo_2C (0.5, 1, 2, 3, 5 wt %) were synthesized. The as-prepared samples were denoted by Mo_2C/TCN-0.5, Mo_2C/TCN-1, Mo_2C/TCN-2, Mo_2C/TCN-3, Mo_2C/TCN-5, respectively. For comparation, the composites consist of Mo_2C and bulk g-C_3N_4 were synthesized by using the same method, named Mo_2C/CN-0.5, Mo_2C/CN-1, Mo_2C/CN-2, Mo_2C/CN-3, Mo_2C/CN-5, respectively.

2.3 Characterization

The crystal structure of these catalysts was measured by X-ray diffraction (XRD) with Cu Kα radiation and the scanning angle (2θ) ranged from 10° to 80°. The Fourier transform infrared (FT-IR) spectra was measured on Bruker Vertex 70 spectrophotometer with samples dispersed in KBr. XPS was analyzed via ESCALAB 250Xi spectrometer with Al Kα radiation source. The morphology and microstructure were determined by Scanning electron microscopy (SEM) and Transmission electron microscopy (TEM). UV–vis absorption (DRS) spectra were performed on a Varian Cary 300 spectrophotometer with an integrating sphere. Photoluminescence (PL) spectra were monitored by a Fluromax-4 spectrophotometer. Time-resolved photoluminescence (TRPL) decay spectra were acquired by a FLS1000 fluorescence spectrometer. (JEOL)JES FA200 spectrometer was used to record the electron spin resonance (ESR) signal. Brunauer-Emmett-Teller (BET) specific surface areas and Barrett–Joyner–Halenda (BJH) pore-size distributions were determined by a nitrogen adsorption analyzer (Micromeritics ASAP 2020, USA).

2.4 Photocatalytic performance evaluation

The photocatalytic performance of these samples was investigated via the degradation of tetracycline (TC) under visible light irradiation. Visible light irradiation was obtained from a 300 W Xenon lamp equipped with a glass filter that could remove the ultraviolet light (λ>420 nm). In each degradation experiment, the catalysts (0.03 g) was thoroughly dissolved in 30 mL TC solution (20 mg L^{-1}). Prior to irradiation, the mixed suspension was under continuous magnetically stirring in dark for 1 h to reach the adsorption-desorption equilibrium between the TC molecules and the catalyst. The concentration of TC was measured by high performance liquid chromatography (HPLC) at its maximum absorbance peak (355 nm) and the injection volume was 20 μL. The HPLC Series 1100 equipped with a UV detector and a C18 reverse-phase column (4.6 × 250 mm) at 30 ℃. The isocratic mobile phase was consist of 80 % water and 20 % acetonitrile with a flow rate of 1.0 mL min^{-1}.

The degradation efficiency (DE, %) of the as-prepared catalysts was calculated by this equation:

$$\eta = \frac{C_0 - C_t}{C_0} \times 100\% \quad (1)$$

Where C_0 and C_t are the initial and t-time concentration of TC solution. The photo-degradation intermediates of TC were determined by liquid chromatography coupled with tandem mass spectrometry (LC–MS/MS) system. Detailed analytic steps were presented in Supplementary Information. In addition, the total organic carbon (TOC) removal efficiency was investigated by the TOC analyzer (Elementar, Germany). To assess the stability of catalysts, the used powders were recycled by filtration, washed with DI water and ethanol, respectively. After dried in an oven, the recovered sample

was used for the cycle experiment. The experimental process was the same as the above-mentioned photocatalytic degradation process.

Moreover, to identify the predominant active species produced in photocatalytic degradation process, radical trapping experiments were carried out with scavengers. For example, $Na_2C_2O_4$, TEMPOL, TBA, which were introduced as quencher of holes (h^+), superoxide radical ($\bullet O_2^-$) and hydroxyl radicals (•OH), respectively. During the photocatalytic reaction, 10 mM scavengers were dissolved in the TC solution. The subsequent operations maintained the same steps as the above photocatalytic degradation experiment.

3. Results and Discussion

3.1 Physicochemical properties

The crystal phase and chemical features of these samples were obtained by XRD patterns and FT-IR spectroscopy. The XRD patterns of Mo_2C and Mo_2C/TCN composite samples were displayed in Fig. 1a and 1b. It can be seen from Fig. 1a that pure Mo_2C exhibited eight obvious diffraction peaks located at 34.35°, 37.97°, 39.39°, 52.12°, 61.52°, 69.56°, 74.64°, 75.51°, corresponding to the (100), (002), (101), (102), (110), (103), (112), (201) planes of the hexagonal β-Mo_2C (JCPDS no. 35-0787) [47]. The analysis result demonstrated the successful fabrication of Mo_2C catalyst. For the specimen Mo_2C/TCN composites (Fig. 1b), all samples exhibited similar peaks at 13.1° and 27.5°, which ascribed to the typical graphite structure. The stronger characteristic peak located at 27.5° is indexed to the (002) plane of TCN, which was associated with

stacking reflection of conjugated planes [49]. The weaker peak of 13.1° was assigned to (100) plane, originating from the repetition of nonplanar units [50]. Compared to CN (Fig. S1), the weaker peak of TCN was ascribed to the ultrathin structure. Apart from the main phase of TCN, the characteristic peaks of Mo_2C can be clearly to see in the Mo_2C/TCN-5 composite specimen, indicating the existence of Mo_2C on the surface of TCN. In the lower content Mo_2C composites, no significant diffraction peak of Mo_2C was found, it may attribute to the small quantity of Mo_2C. Fig. 1c showed the FT-IR spectra of the CN, TCN and Mo_2C/TCN composite samples. All samples have the typical peaks of g-C_3N_4. In detail, the band that appeared at 810 cm^{-1} was originated from the bending vibration or breathing mode of triazine units. The series of peaks in 1600~1200 cm^{-1} region dominated the spectrum, could be corresponded to the typical stretching vibration modes of aromatic heterocycles. The broad absorption peaks between 3600~2900 cm^{-1} were identified to be the N-H in terminal amine groups. The composite samples retained the same framework with the FT-IR spectra of TCN and no significant peaks altered, demonstrating the molecular structure of TCN has not changed after loading Mo_2C particles.

Journal Pre-proofs

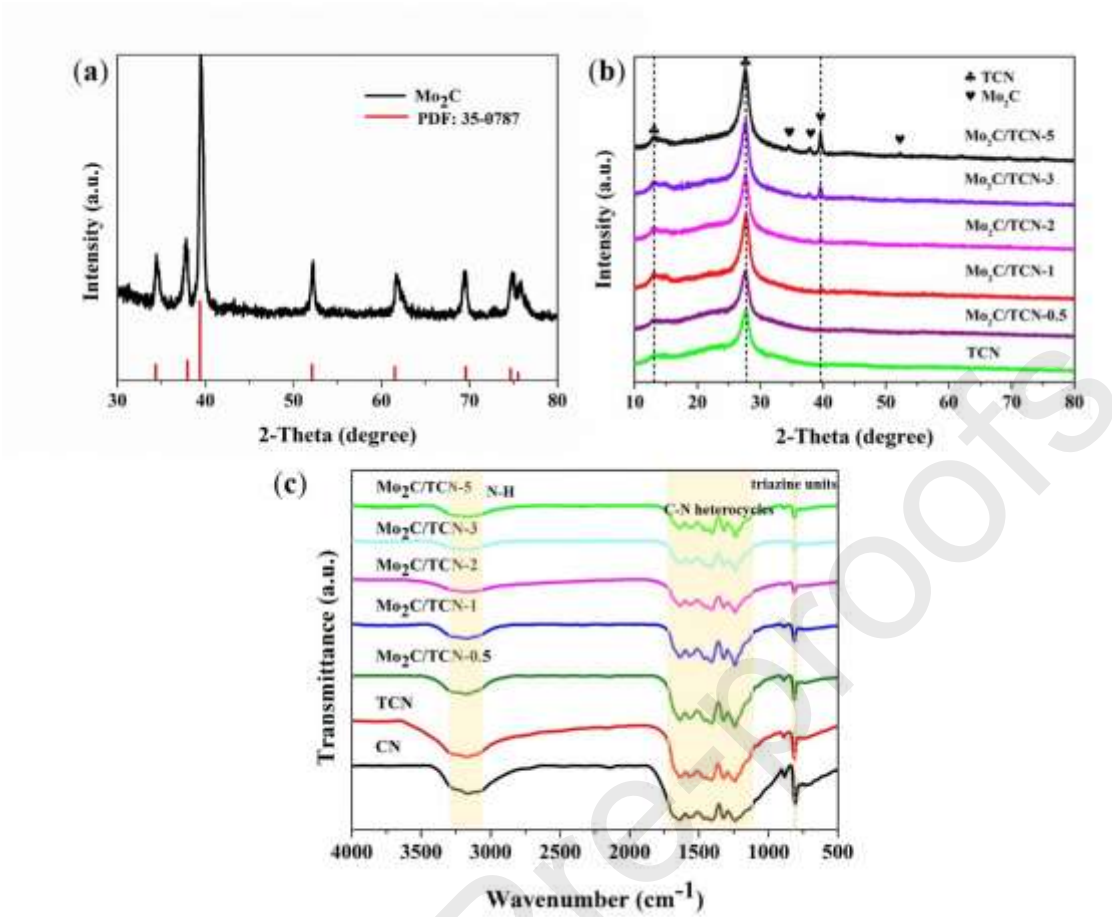

Fig. 1. XRD patterns of (a) Mo_2C and (b) TCN, Mo_2C/TCN samples; (c) FT-IR spectra of CN, TCN and Mo_2C/TCN sample.

The composition and chemical state of the Mo_2C, TCN and Mo_2C/TCN-2 were characterized by using XPS technique. The overall XPS survey spectrum was exhibited in Fig. 2a, four chemical elements of C, N, O and Mo were clearly displayed on the surface of Mo_2C/TCN-2 catalysts. Obviously, there was only XPS peak of C, N and O element in the measured spectrum of TCN. The oxygen region might originate from the chemisorbed oxygen on the materials surface and the residual oxygen from the urea polymerization process [51]. The high-resolution XPS spectra of C 1s, N 1s and Mo 3d were recorded in Fig. 2b-d. The C 1s spectrum of TCN can be deconvoluted into two peaks with binding energies at 288.2 and 284.8 eV. The first peak at 288.2 eV was

associated with sp^2-hybridized C from the N–C=N bond [52], and the latter peak with low intensity at 284.8 eV was assigned to alkyl or adventitious carbon [53]. Comparatively, C 1s peaks in Mo_2C/TCN-2 slightly shifted to higher binding energies after loading Mo_2C particles. For N 1s spectra of TCN, three fitted peaks located at around 398.8, 399.6, 400.9 eV, corresponding to sp^2 hybridized aromatic N in triazine rings (C=N-C), tertiary nitrogen N-$(C)_3$ groups, and terminal C-N-H amino functions, respectively [54, 55]. Compared with TCN, the new binding energy at 396.8 eV of Mo_2C/TCN-2 was assigned to Mo-N bond [56, 57]. The new bond altered the charge distribution and enhanced the intimate contact between Mo_2C and TCN. The Mo-N bonds formed at the interface was crucial to the separation of electrons, which providing a transfer high-pathway for electrons to reach the active site and participating in further redox reaction. It was worth noting that the N 1s peaks in Mo_2C/TCN-2 shifted about 0.3 eV toward the higher binding energy, which might be attribute to the strong interaction between Mo_2C and TCN. Because of spin–orbital coupling, the Mo 3d XPS spectrum are split into 3d5/2 and 3d3/2 peaks. The Mo 3d XPS peak of Mo_2C can be fitted using three deconvoluted doublets, Mo_2C (d5/2 at 228.1 eV, d3/2 at 231.6 eV), MoO_3 (d5/2 at 232.3 eV, d3/2 at 235.5 eV) and MoO_2 (d5/2 at 229.2 eV, d3/2 at 232.6 eV) [58-60]. The oxides were arising from the superficial oxidation of Mo_2C, which was inevitably when exposed to air, as evidenced by the previous literature [61]. It was worth noting that the Mo 3d XPS peak of Mo_2C/TCN-2 obvious shifted to more negative energy zone than pristine Mo_2C. Obviously, the C 1s and N 1s peaks of TCN changed to higher binding energies after hybridization with Mo_2C, while the binding

energies of Mo 3d of Mo_2C/TCN-2 were lower than those of Mo_2C. According to the change of binding energy, it was reasonable to assert that the electron density within Mo_2C nanoparticles increased after hybridization with TCN, as reported in previous literatures [62, 63]. The partial electron transferred from electron-rich TCN to Mo_2C, leading to the electron density of Mo_2C increase and then the binding energies of Mo 3d decrease [64-66]. In other words, the electrons were transferred from TCN to Mo_2C in Mo_2C/TCN photocatalytic system. The well-matched band potentials of the Mo_2C/TCN were consistent with the conditions for constructing direct Z-scheme photocatalytic system. These results were evidenced by the different flat band potentials, as introduced in the following section. The obtained TCN with narrow band gap of 2.43 eV and the estimated flat potential by using Mott-Schottky (M–S) method was -0.57 eV vs NHE. And the flat potential of Mo_2C is -0.87 eV vs NHE, which was more negative than that of TCN. So, the electrons could not transfer from the conduction band (CB) of TCN to the CB of Mo_2C. That is to say, the type-II heterojunction charge transfer model was impractical in the Mo_2C/TCN system. Therefore, the Z-scheme heterojunction system between Mo_2C and TCN was proposed.

Journal Pre-proofs

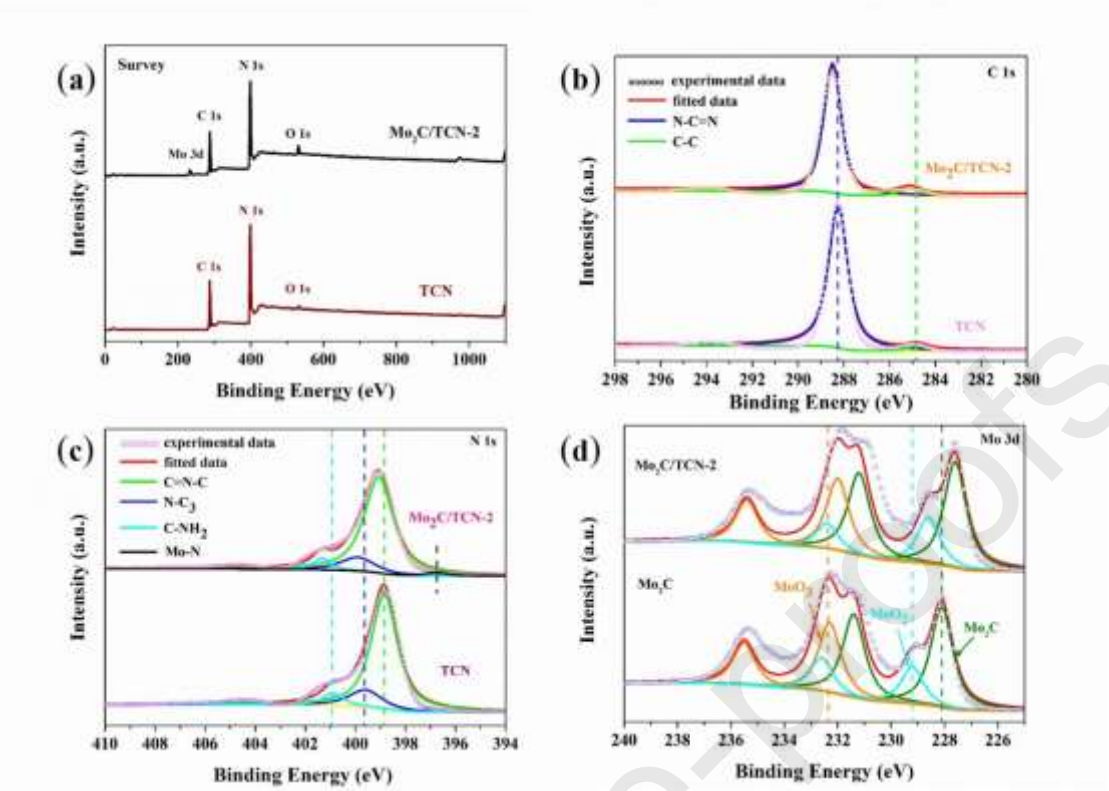

Fig. 2. XPS spectra of Mo_2C/TCN-2 photocatalyst: (a) a survey spectrum; high-resolution spectra of (b) C 1 s, (c) N 1 s and (d) Mo 3d. Mo_2C: green, MoO_2: blue, MoO_3: orange.

In this research, the morphology and structure of Mo_2C, TCN and Mo_2C/TCN composite catalysts were further investigated by SEM and TEM. As observed in Fig. 3a and 3d, the Mo_2C crystals consist of nanobelt structures .The high resolution TEM (HRTEM, Fig. S2c) revealed that the Mo_2C with inter planar distance of 0.23 nm and 0.26 nm, which might be indexed to the (101) and (100) plane [63]. This result correlated well with XRD analysis. The SEM image (Fig. 3b) showed the hollow tubular like growth of g-C_3N_4. It was obvious in the SEM image that the tubular structures were dense with variegated diameter. The TEM studies (Fig. 3e) were carried out to further observe the hollow tubular morphology. It was clearly that the TCN with

thin tubular structure. This hollow tubular structure leads to high specific surface area, offers more active sites for surface reactions and facilitates photo-induced electrons transfer in a shorter distance, thus effectively improving the charge separation and transfer efficiency [67]. The structure of Mo_2C/TCN-2 composite catalysts was presented in Fig. 3f. Fig. 3f showed a TEM image of Mo_2C/TCN with the close contact between TCN and Mo_2C. It was obvious that the TCN maintained the hollow structure with the deposition of Mo_2C. From the HRTEM image of Mo_2C/TCN-2 shown in Fig. 3g, it was obvious that the lattice fringes of Mo_2C coupled with the fringes of TCN, indicating the tightly contact of the two semiconductors. Furthermore, the energy dispersive spectroscopy (EDS) elemental mapping images of Mo_2C/TCN-2 (Fig. 3h) identified the presence of C, N, Mo elements, which were uniformly distributed within the TCN matrix. In addition, the Energy Dispersive X-Ray Fluorescence Spectrometer (EDX) analysis was shown in Fig. S2d. These results clearly stated the intimate contact between Mo_2C and thin-wall TCN, which greatly facilitating the separation and transfer of photo-induced charge carriers.

Journal Pre-proofs

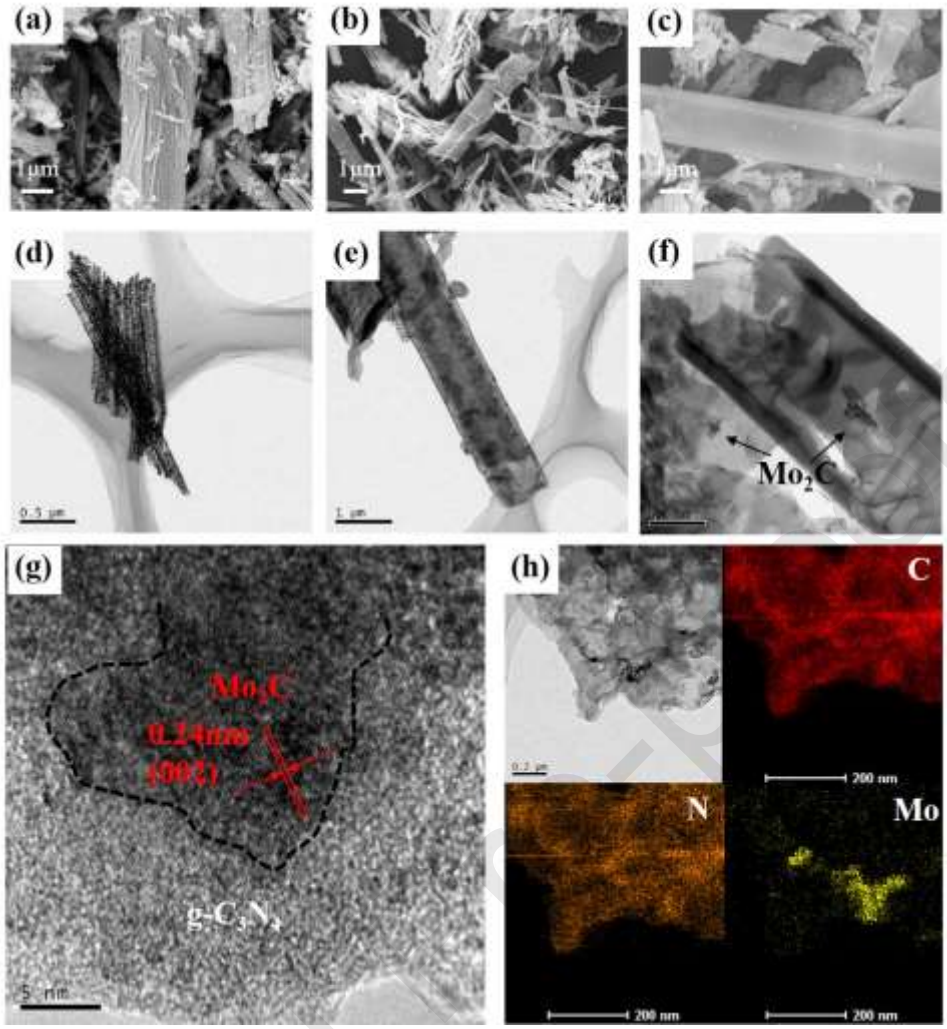

Fig. 3. SEM images of samples of (a) Mo_2C, (b) TCN, and (c) Mo_2C/TCN-2, respectively. TEM images of samples of (d) Mo_2C, (e) TCN, and (f) Mo_2C/TCN-2, respectively. (g) HRTEM images of the Mo_2C/TCN-2 and (h) EDS elemental mapping for C, N, Mo elements over the Mo_2C/TCN-2 photocatalyst.

UV-vis diffuse reflectance spectroscopic experiments were conducted to investigate the optical properties of CN, TCN, and Mo_2C/TCN samples. As shown in Fig. 4a, pristine CN exhibited intrinsic steep absorption edge at 450 nm [68]. In contrast, Mo_2C showed strong light absorption in the wavelength range from 300 to 800 nm. In addition, the photo-absorption ability of Mo_2C/TCN composites demonstrated

significant enhancement with increasing of Mo_2C content, corresponding to the color alteration from light yellow to yellowish green. With the addition of Mo_2C, the much enhanced visible light absorption capability of composite photocatalyst can be observed, indicating the efficient sensitization effect of Mo_2C on TCN [69]. The light harvesting efficiency of photocatalysts played a key role in solar energy conversion, suggesting the Mo_2C/TCN composite materials have great application prospects in the field of photocatalysis. By applying Kubelka-Munk method [70], the band gap energy (E_g) of CN, TCN and Mo_2C can be estimated by the plot of $(\alpha h\upsilon)^{1/2}$ against photo energy ($h\upsilon$), as Fig. 4b and Fig. S3a shown. The calculation formula is shown as follows:

$$\alpha h\upsilon = A(h\upsilon - E_g)^{n/2} \quad (2)$$

Where α, h, υ, A are corresponding to the absorption coefficient, Planck constant, light frequency and proportionality constant, respectively. The index n is determined by the interband transition mechanism, and the value is equal to 1 for a direct-gap material. As a result, the calculated E_g of Mo_2C (Fig. S3a), TCN and CN (Fig. 4b) were recorded to be 1.58 eV, 2.43 eV, and 2.62 eV, respectively. Mott-Schottky (M–S) plots were performed in this research to determine the electronic structures and semiconductor types for CN, TCN and Mo_2C catalyst at frequencies of 1000 Hz in 0.2 mM Na_2SO_4. As illustrated in Fig. 4c and Fig. S3b, the positive slopes of M–S curves implied their n-type semiconductor character [71]. The estimated flat potentials of CN, TCN (Fig. 4c) and Mo_2C (Fig. S3b) were -0.83 eV, -0.77 eV, and -1.07 eV versus Ag/AgCl electrode (i.e. -0.63 eV, -0.57 eV, and -0.87 eV vs. normal hydrogen electrode (NHE) [72]), respectively. For n-type semiconductor, it was generally accept that the CB potential

(E_{CB}) was more negative by about -0.2 V than that of flat potential [73]. Thus, the E_{CB} for CN, TCN and Mo_2C were speculated to be -0.83 eV, -0.77 eV, and -1.07 eV vs. NHE, respectively. The valence band (VB) potentials (E_{VB}) can be calculated by the equation: $E_{VB} = E_{CB} + E_g$. Therefore, the E_{VB} of CN, TCN and Mo_2C are 1.79 eV, 1.66 eV, and 0.51 eV vs. NHE. The calculated edge positions and band structure of CN, TCN and Mo_2C were shown in Fig. 4d.

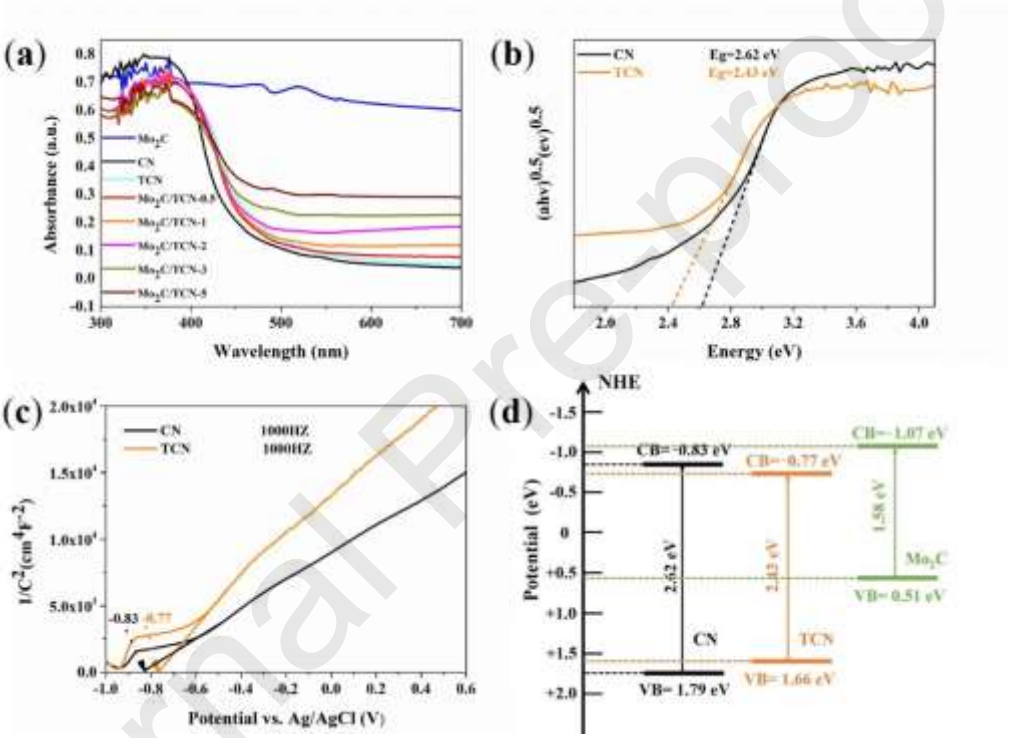

Fig. 4. (a) UV–vis diffusion reflection spectra of CN, TCN, Mo_2C and Mo_2C/TCN samples; (b) bandgap and (c) Mott-Schottky plot of CN, TCN; (d) band structure diagrams for CN, TCN, and Mo_2C.

3.2 Photo-induced charge transfer ability

To investigate the properties of charge carrier recombination together with the role of Mo_2C in the photocatalytic process, a series of photoelectrochemical analysis were

conducted. Steady-state photoluminescence (PL) technique and time-resolved photoluminescence (TRPL) can be used to depict the process of charge carrier trapping, separation, migration and transfer. In principle, the fluorescence emission peak were generated when radiative recombination of charge carriers occurred and the higher PL signal represented higher recombination efficiency [74]. As shown in the Fig. 5a, the PL intensity of the Mo_2C/TCN composite was much weaker than that of pristine TCN, indicating the efficient separation of photo-generated electron/hole pairs was accelerated and the recombination of charge carriers was inhibited at the hetero-interface between Mo_2C and TCN. The Mo_2C served as electrons trapping center, facilitating the transfer of electrons which generated in the surface of TCN, thus the composite samples exhibited low recombination rate of electron/hole pairs. Fig. 5b recorded the fluorescence decay curves over CN, TCN and Mo_2C/TCN-2 hybrid, which were fitted based on the bi-exponential decay function [75]:

$$I(t) = B_1\exp(-t/\tau_1) + B_2\exp(-t/\tau_2) \quad (3)$$

Where τ_1 and τ_2 are the fluorescent lifetime for the slower and faster components, and B_1, B_2 are the corresponding amplitudes. As can be seen in the table (Fig. 5b right inset), both the short lifetime component τ_1 and long lifetime component τ_2 of Mo_2C/TCN-2 were prolonged compared to the TCN and CN. As a result, the Mo_2C/TCN-2 displayed a longer average lifetime (τ_{ave}). The longer emission lifetime confirmed a faster charge transfer process in Mo_2C/TCN-2 nanotube and the formed heterojunction interface effectively depressed the charge recombination, thus elongating the lifetime of

photogenerated charge carriers [76, 77]. Here, the τ_{ave} was calculated by applying the Eq [78]:

$$\tau_{ave} = \frac{B_1\tau_1^2+B_2\tau_2^2}{B_1\tau_1+B_2\tau_2} \quad (4)$$

To provide additional evidences for the excellent ability of Mo_2C/TCN composites to promote the interfacial charge separation, the transient photocurrent measurement and EIS technologies was performed. The photoresponses of CN, TCN and Mo_2C/TCN-2 electrodes without external bias under visible light irradiation were shown in Fig. 5c. As illustrated in the amperometric I-t curves, the transient photocurrent can be observed once the light turned on due to the separation of photo-induced carries. Besides, after loading of Mo_2C, the photocurrent response density of Mo_2C/TCN-2 increased distinctly and was about 2 times than that of pristine CN, suggesting the significant enhancement of charge separation efficiency. Mo_2C exhibited ultrahigh electrical conductivity and minimized the charge transport resistance [79, 80]. The high electrical conductivity possessed powerful driving forces to induce electron transfer from the surface of TCN to the inner interface of Mo_2C. The internal electrostatic field formed at the hetero-interface between the TCN and Mo_2C contributed to the efficient separation of photo-induced electron/hole pairs [77]. EIS Nyquist plots of CN, TCN and Mo_2C/TCN-2 were obtained in Fig. 5d. In contrast to pure CN and TCN, the arc radius of Mo_2C/TCN-2 was much smaller, demonstrating the transport resistance reduced after loading Mo_2C particles. This result was corresponding with the photocurrent measurement. The decreased transport resistance

realized fast interfacial charge migration, leading to the enhancement of photocatalytic performance.

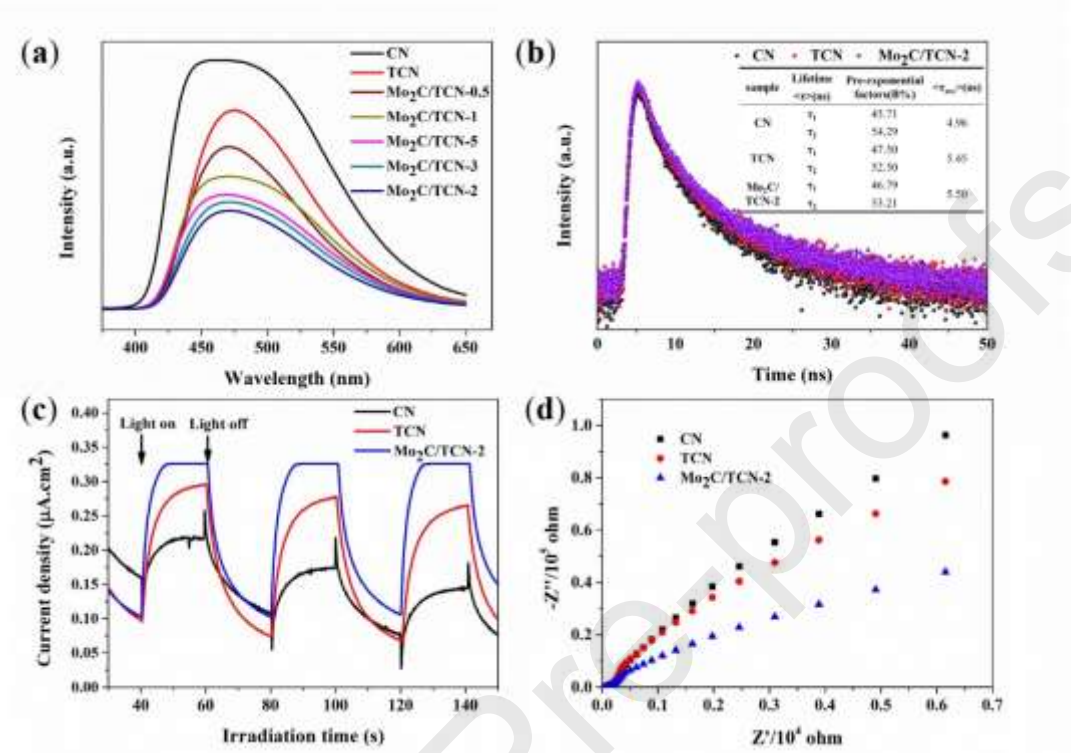

Fig. 5. (a) Steady-state photoluminescence spectra of the as-prepared samples; (b) time-resolved photoluminescence decay spectra and (c) transient photocurrent response curves and (d) Nyquist plots of electrochemical impedance spectroscopy of CN, TCN and Mo_2C/TCN-2 photocatalysts.

3.3 Photocatalytic performance

3.3.1 Adsorption and photocatalytic properties

The ability of photocatalysts to adsorb target contaminants is one of the decisive factors affecting photocatalytic efficiency. Adsorption of TC by Mo_2C/TCN composites without photo-reduction was carried out to investigate the adsorption capacity. It can be seen from Fig. 6a, the Mo_2C exhibited relatively large adsorbed amount of the target

contaminants when the adsorption equilibrium is reached after 1 h. The maximum adsorption amount was 8.13 mg g^{-1}, attributing to the excellent adsorption properties and attractive surface charge of Mo_2C. In addition, the doped Mo element in the composites provided valence electrons, facilitating the bonding of the TC molecule to the metal center [81]. Therefore, with increasing content of Mo_2C, the adsorption capacity of the Mo_2C/TCN composite material was significant enhanced. It was apparent that the adsorption-desorption equilibrium between Mo_2C and TC molecules reached within 60 min. Accordingly, before visible light irradiation, the TC solution was churned for 1 h under dark condition to establish the adsorption equilibrium. The pseudo-first-order, pseudo-second-order models were examined to investigate the adsorption process of TC molecules by the obtained samples (Fig. 6b and 6c). The detailed experimental data were shown in Table S1. The values of correlation coefficient obtained by the pseudo-second-order kinetic mode were much higher than the pseudo-first-order kinetic mode. So the pseudo-second-order kinetic mode was more suitable to describe the adsorption behavior of TC, indicating the TC adsorption was much affected by chemical mechanism [82]. In order to illustrate adsorbate-adsorbent interaction, the isotherm models such as Freundlich and Langmuir isotherm equations were used [83]. The adsorption isotherm expressed reaction behavior between the concentration of adsorbate Ce (mg L^{-1}) and the adsorption capacity of adsorbent qe (mg g^{-1}) at constant temperature. As shown as Fig. 6d and Table S2, the experimental data showed good correlation with Freundlich model, implying the adsorption energy decreased exponentially at the finishing point of adsorbent

adsorption center [84]. The Freundlich equilibrium isotherm model was used for the description of molecules multilayer adsorption and the high R^2 (0.9983) manifested the strong interaction between Mo_2C and TC molecules. The increased adsorption capacity and the hollow tubular structure of Mo_2C/TCN motivated us to inspect its BET surface area and pore size distribution information. The as-prepared CN, TCN, Mo_2C and Mo_2C/TCN-2 were investigated by the nitrogen adsorption-desorption isotherm experiments and corresponding BJH pore-size distributions, as displayed in Fig. 7. The pore size distribution curves can be seen in the inset of Fig. 7. The BET specific surface areas of CN (14.414 m^2/g), Mo_2C (23.744 m^2/g), TCN (25.139 m^2/g) and Mo_2C/TCN-2 (28.542 m^2/g) were measured to be increased in turn. Mo_2C/TCN-2 possessed the highest BET surface area, showing a 2.5 times higher than bulk CN and 1.14 times higher than TCN. The introduction of Mo_2C provided more active sites, thus increasing the specific surface area of the composite. These results further highlighted the hollow tubular structure of TCN as well as the tightly coupled of Mo_2C and TCN, in agreement with TEM results.

Journal Pre-proofs

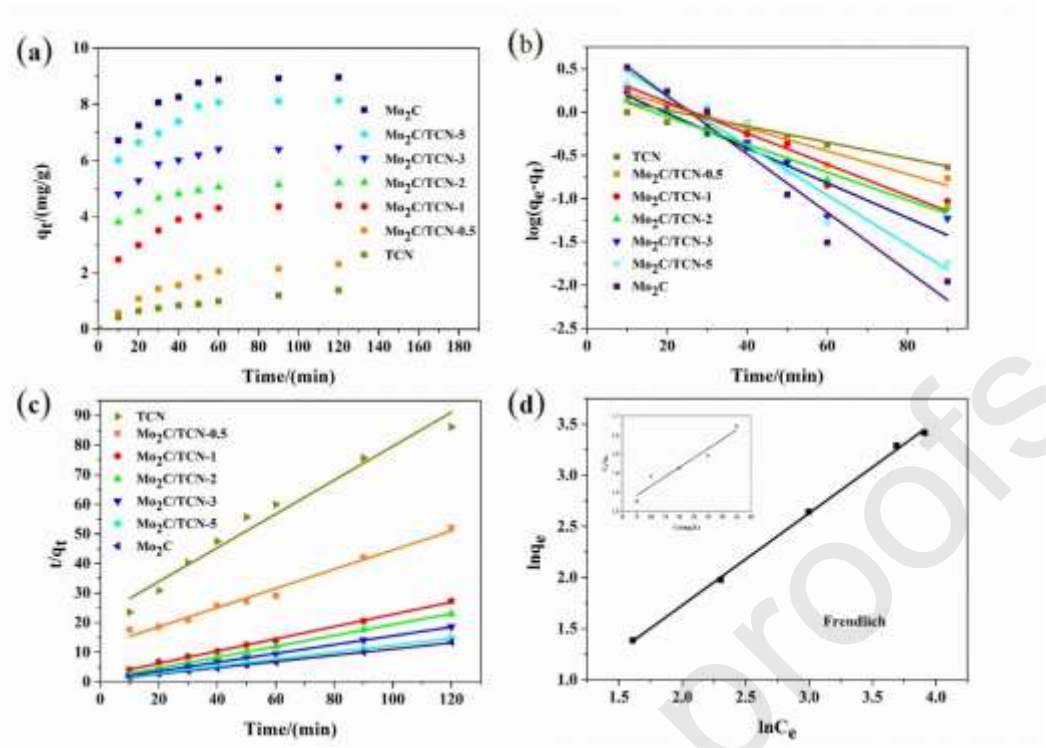

Fig. 6. (a) Effect of contact time on the adsorption of TC onto Mo_2C/TCN-2 under darkness; (b) the pseudo-first-order plots; (c) pseudo-second-order plots; detail equilibrium isotherms: (d) Freundlich model and Langmuir model (inset) for TC adsorption by Mo_2C/TCN-2 under darkness.

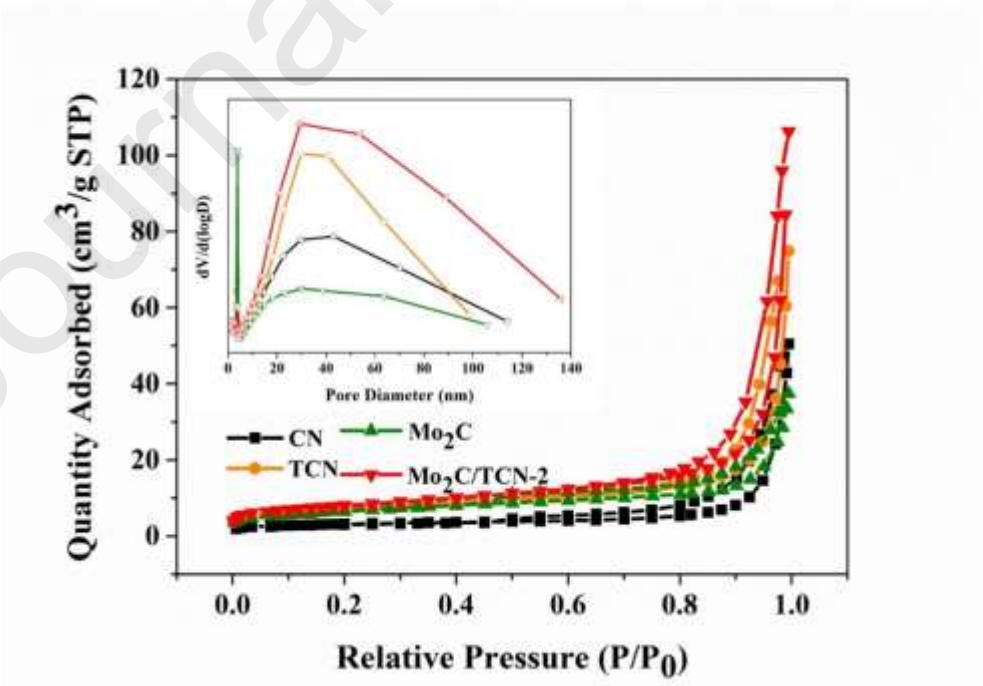

Fig. 7. Nitrogen adsorption-desorption isotherms and the pore size distribution curves (insert) for CN, TCN, Mo_2C and Mo_2C/TCN-2.

For the photocatalytic process, all samples undergone 1 h dark absorption before exposing to visible light. Without the presence of photocatalyst, the natural photolysis of TC solution was negligible, indicating the TC solution with high stability under visible light. Fig. 8a depicted the change in TC removal efficiency with irradiation time over the CN, TCN and Mo_2C/TCN series photocatalyst under visible light irradiation. Compared with the low degradation efficiency of pure TCN (55.9 %) and CN (26.2 %), all the Mo_2C/TCN series showed significant enhanced photocatalytic activity, in an order of Mo_2C/TCN-2 > Mo_2C/TCN-3 > Mo_2C/TCN-5 > Mo_2C/TCN-1 > Mo_2C/TCN-0.5. The Mo_2C/TCN-2 photocatalyst demonstrated the highest photocatalytic degradation efficiency of 91.6 %. The loading of Mo_2C nanoparticles seemed to inspire the photocatalytic ability of TCN. With an increasing proportion of Mo_2C, the TC degradation efficiency of TCN exhibited an increasing trend. The enhancement of photocatalytic activity should be ascribed to the better adsorption capacity for TC molecules, the wider spectral range for photo-absorption and the high efficiency of electronic charge transport. However, as the Mo_2C contents further increased to exceed the optimal proportion, the photocatalytic performance of TCN decreased. An excess Mo_2C will mask the active spots for contaminant reduction and decrease the light harvesting ability. In addition, the high amount of Mo_2C loading could result in the introduction of recombination centers, leading to the rapid electron-holes recombination [85]. For comparation, the removal efficiencies of TC over Mo_2C and

Mo_2C/CN-x were presented in Fig. S4. The introduction of Mo_2C in the Mo_2C/CN composite was likely to inspire the improvement of photocatalytic ability, which was in good consistent with the observation of Mo_2C/TCN-x photocatalytic system. The apparent rate constant (k) was used to quantitatively characterize the TC degradation reaction kinetic. The experimental data were expressed as the following equation:

$$ln(C_0/C) = kt \quad (5)$$

As displayed in the kinetic curves (Fig. 8b), the Mo_2C/TCN-2 denoted the highest degradation rate constant with the value of 0.0391 min^{-1}, which was about 3 times and 9 times than TCN and pristine CN. The excellent photocatalytic performance of Mo_2C/TCN-2 can be attributed to the co-effects in the enhancement of adsorption capability and electrons transport efficiency. The above results revealed the efficient composition ratio between Mo_2C and TCN, thus the Mo_2C/TCN-2 nanocomposite photocatalyst was used in subsequent experiments.

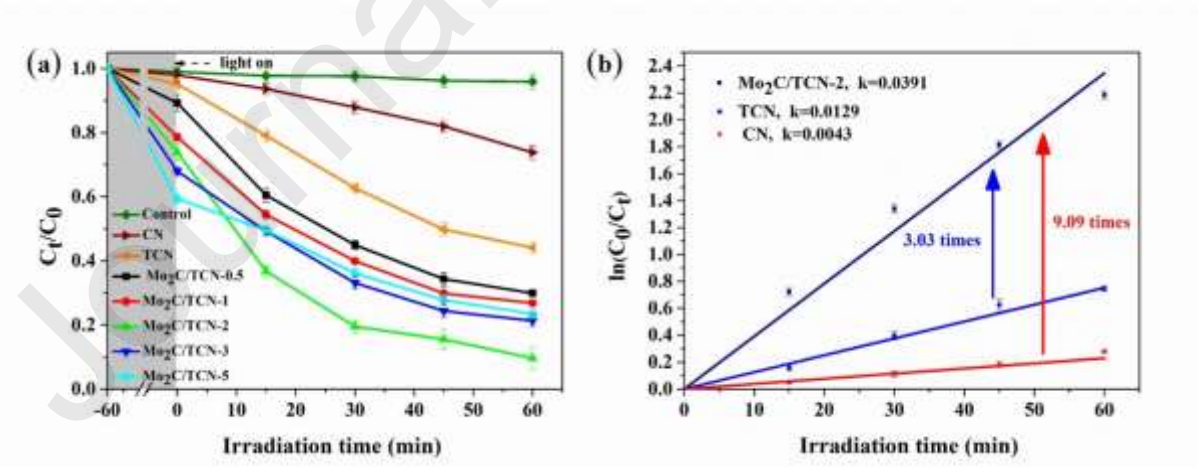

Fig. 8. (a) Removal of TC in the presence of different photocatalysts with various composition ratios between Mo_2C and TCN under visible light irradiation; (b) photocatalytic rate of Mo_2C/TCN-2 under visible light irradiation.

3.3.2 Effect of initial TC concentration

Effect of initial TC concentrations were also investigated to test the photocatalytic activity of samples, shown as Fig. 9a. On the whole, all the obtained Mo_2C/TCN series photocatalysts showed good TC removal efficiency with different initial TC concentrations (5–40 mg L^{-1}) due to the excellent adsorption performance. And the removal efficiency increased with a decrease of the initial TC concentrations. The result may be explained that the higher concentration pollutants would cause less active sites to decrease photon absorption and the more generated intermediates would consume photogenerated electrons, leading to lower photocatalytic activity [86].

3.3.3 Effect of supporting electrolytes

The inorganic salt ions, such as SO_4^{2-}, Cl^-, HCO_3^-, coexistence in real water, might affect the photocatalytic performance of the catalyst. The electrolytes would interfere the degradation process of pollutants via competing the active site on the surface of photocatalysts. To explore the practical application of photocatalysts, the effect of supporting electrolytes was investigated, as shown as Fig. 9b. The electrolyte solutions of NaCl, Na_2CO_3, NH_4Cl, and Na_2SO_4 were at a concentration of 0.05 M. The four model inorganic salts exhibited different TC removal rates, with an order of NaCl > NH_4Cl > Na_2SO_4 > Na_2CO_3. With the addition of extra ions, the adsorbed amount of TC decreased slightly, accounting for the following reason: the salt would promote protonation and lead to electrostatic interaction between electrolyte ions and TC^+ ions, thus facilitating the dissociation of TC molecules toward TC^+ [87]. Na^+ ions have been proved to have little effect on the degradation of TC [88], while the slightly decreases

of TC remove amount was detected in the presence of NaCl, maybe originated from the occupation of actives sites by Cl^-. The removal rate of TC was strikingly hampered with the presence of Na_2CO_3 and Na_2SO_4. Na_2CO_3 was regarded as pH buffers and it was able to alkalinize solution, leading to the enhancement of electrostatic repulsion between TC molecule and the catalyst, thus affecting the adsorption of TC molecules to the catalyst surface. In addition, $HCO_3^-$and SO_4^{2-} are two effective free radical scavenger, the radical species generated at the photocatalysts surface and subsequently trapped by the coexisting $HCO_3^-$and SO_4^{2-} [89]. The reduction of radical species great inhibited the photocatalytic efficiency.

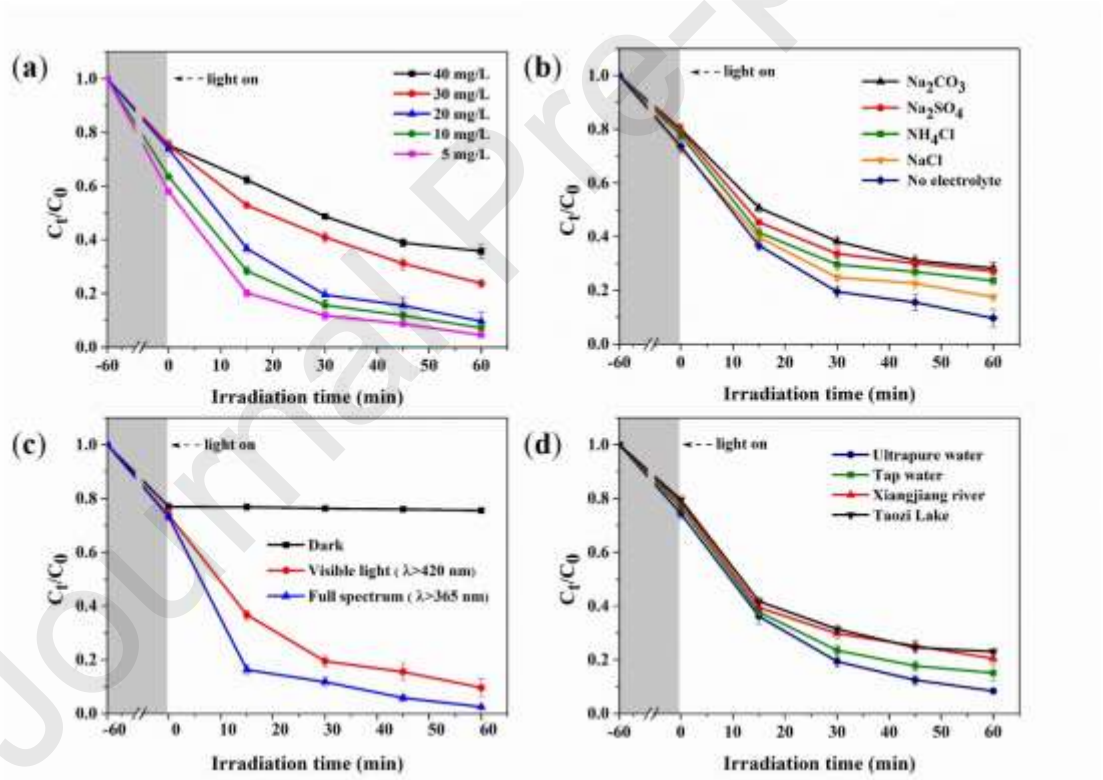

Fig. 9. (a) Effect of initial TC concentrations; (b) supporting electrolytes; (c) light sources and (d) different water samples condition on the photocatalytic degradation of TC in the presence of Mo_2C/TCN-2 photocatalysts.

3.3.4 Effect of light irradiation condition

Solar light produces radiation of different energies that affects the performance of photocatalytic contaminant removal. The dark condition, visible light irradiation condition ($\lambda > 420$ nm) and full spectrum irradiation condition ($\lambda > 365$ nm) were created to the effect of light irradiation on photocatalytic efficiency of Mo_2C/TCN-2 photocatalysts. Fig. 9c displayed TC concentration change under different light illumination conditions. Without light irradiation, the TC concentration showed no striking decline except for the adsorption loss. It was notably that the concentration of TC was close to zero after 1 h full spectrum irradiation and photodegradation efficiency of TC reach to 91.6 % under visible light irradiation. This means shorter wavelength with greater photon energy which facilitating the separation of electron-hole pairs, thus enhancing the photocatalytic performance [90].

3.3.5 Application on real water samples

Water matrix is an important factor for the practical application of papered composites. Various ions are present in natural water matrix [91]. Therefore, we investigated the effect of different water matrixes (ultrapure water, tap water, lake water and river water) for the photocatalytic degradation of TC in the presence of Mo_2C/TCN-2 photocatalysts. The sampling sites were shown in Fig. S5. The initial concentration of TC was 20 mg/L. As can be seen from Fig. 9d, the adsorption and photodegradation processes of Mo_2C/TCN-2 photocatalysts in various medium exhibited different response. The adsorbed amount of TC in actual natural water was relatively decreased compare to the ultrapure water and the photocatalytic efficiency of TC degradation in

an order of ultrapure water (91.62 %) > tap water (84.84 %) > river water (79.82 %) > lake water (76.8 %). According to the parameters characteristics of water sources (Table S3), we can see the pH value and co-exist ions concentration varies among different water samples. The pH value effected the TC surface charge interaction for adsorbing onto the surface of catalysts [92, 93]. The coexisting metal ions may contribute to the absorption by bridging the material surface and TC molecule [82]. On the other hand, the ions contained in the natural water may compete with TC molecules for the active sites, resulting to the decreased photocatalytic activity. In summary, the photodegradation of TC over Mo_2C/TCN-2 still remain high efficiency in actual natural water.

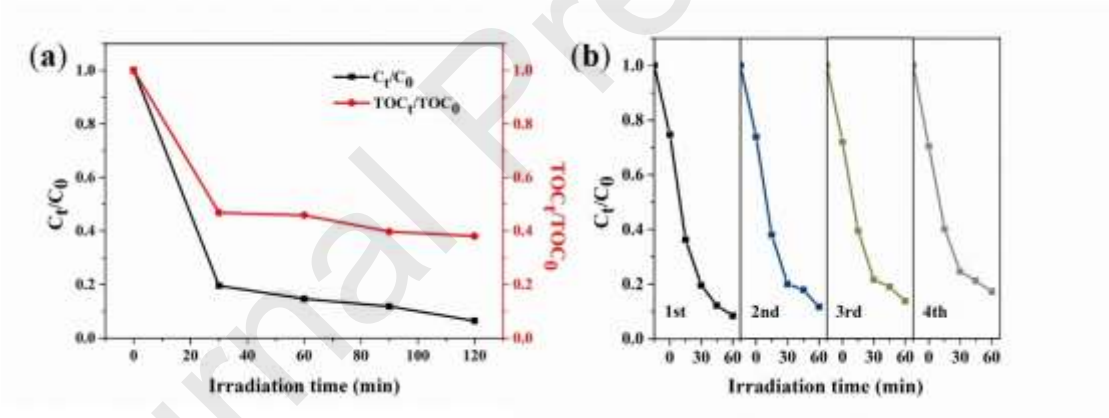

Fig. 10. (a) The photocatalytic degradation and TOC removal curves of TC on Mo_2C/TCN-2 photocatalysts. (b) The cycling test for the degradation of TC by the fresh and used Mo_2C/TCN-2 catalysts.

3.3.6 Mineralization of TC and stability of Mo_2C/TCN-2

The ability to mineralize organic pollutants is critical for removing environmental pollution. To deeper evaluate the mineralization property of Mo_2C/TCN-2 photocatalysts, total organic carbon analyzer (TOC) was used under optimized

experimental conditions. As shown in Fig. 10a, within 2 h visible light irradiation, the degradation and mineralization efficiency of TC reached to 93.6 % and 61.91 %. The result demonstrated that Mo_2C/TCN-2 exhibited favorable mineralization ability. Practical applications required photocatalytic materials with advantageous recyclability and excellent chemical stability for the aim of saving costs and refraining from secondary pollution. To discuss the stability of catalysts, the photocatalytic experiment of Mo_2C/TCN-2 nanomaterial had been performed four reaction runs. As shown in Fig. 10b, compare to fresh catalysts, the used Mo_2C/TCN-2 photocatalysts exhibited little inhibition in TC degradation. After four-round continuous reaction, the photodegradation efficiency of TC maintained 82.8 %, indicating the photocatalysts were stable during the photodegradation process. In addition, the used sample was characterization by FT-IR, XPS and XRD, shown as Fig. S6. These analyses further demonstrated the stability of the as-obtained sample.

3.3.7 Possible degradation pathway of TC

Characterizing the intermediates formed in the TC photocatalytic degradation process is beneficial to deepen the understanding of its degradation pathway and mechanism. The degradation intermediates of TC over Mo_2C/TCN-2 were identified by LC-MS/MS.

The corresponding MS spectra of possible intermediates are displayed in Fig. S7. The mass to-charge ratio (m/z) of 445.2 was deemed to parent TC [94]. The intensity of TC peak gradually weakened as the degradation progresses, indicating the destruction of TC molecular. Based on the emerged intermediate products and the

previous reports, the potential degradation pathways of TC were illustrated in Scheme 1. According to the molecular structure of intermediates, the transformation intermediates resulted from the following reaction: hydroxylation; the elimination of amide group, carboxyl, ketone group, N-methyl; and substitution ring-opening reaction. The TC molecular was firstly transformed to the product 1 (m/z = 417) via the N-demethylation process, due to the low energy of the N-C bond [95]. And then the product 1 was attacked by the •OH to form hydroxylated product 2 (m/z = 432). Product 2 could further decompose during oxidation reaction. The reactive species attacked C_{6a}–C_7 bond of aromatic ring, leaving behind a ketone and a carboxylic group [96-98]. Thus the product 3 (m/z = 481) generated and it was further oxidized to simpler product 4 (m/z = 305). •O_2- and h^+ as the major active species successive attacked product 1. The ion fragmentation formed in the following order during collision-induced dissociation: product 5 (m/z = 362) generated by deamination and deacylation; via cleavage of the carboatomic ring, product 6 formed (m/z = 318); product 7 (m/z = 274) was stemmed from the decarboxylation of product 6 [99, 100]. On the other hand, product 8 (m/z = 383) were formed through deacylation reaction after the dehydration of the TC molecular [101]. The opening ring product 9 (m/z = 359) was formed through the further oxidation of product 8. The produced intermediates were further decomposed to low-molecular weight organic compounds and finally oxidized into CO_2 and H_2O [100, 102].

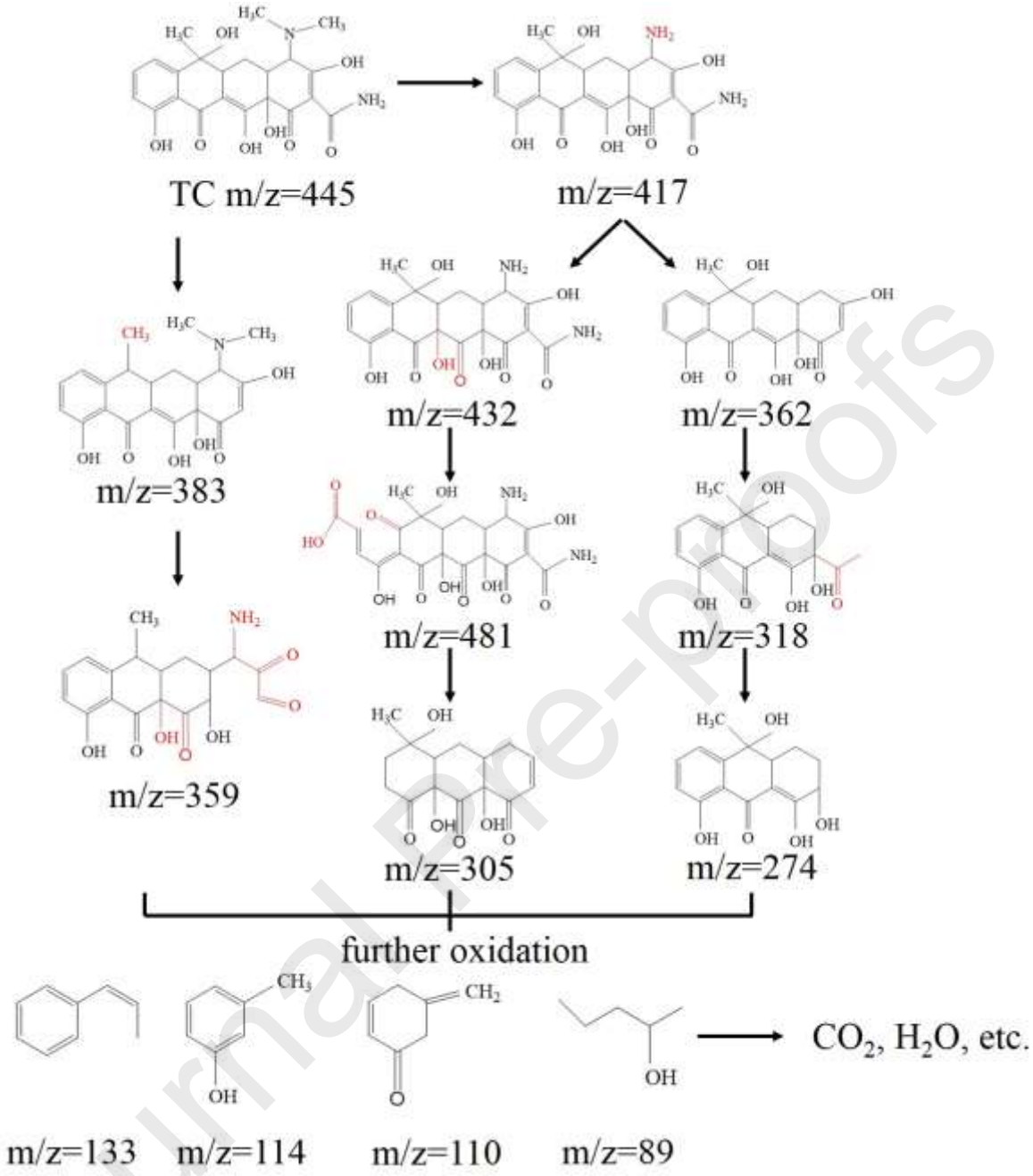

Scheme 1. Proposed photocatalytic degradation pathways of TC.

3.4 Photocatalytic mechanism

In order to investigate the photocatalytic mechanism, trapping experiments were carried out to determine the reactive species formed in the photocatalytic degradation process. In the photocatalytic system, we considered $\bullet O_2^-$, holes (h^+) and hydroxyl

Journal Pre-proofs

radicals (•OH) by adding 10 mM TEMPOL, $Na_2C_2O_4$ and TBA as scavengers, respectively [103, 104]. As presented in Fig. 11a and 11b, the photocatalytic activity deterioration significantly in the presence of TEMPOL and $Na_2C_2O_4$, the degradation efficiency of TC only reached to 29.94 % and 34.05 %, indicating that the $\bullet O_2^-$ and h^+ were both active species in the decomposition process of TC. While a slight decrease of TC degradation rate of 19.3 % was observed with the introduction of TBA, suggesting that •OH also participated in TC photocatalytic degradation process. In summary, the active species involved played an important role in the photocatalytic reaction process by the order of $\bullet O_2^- > h^+ >$ •OH. Therefore, the main active species contributed to the removal of TC were $\bullet O_2^-$ and h^+, •OH acted as an assistant. In order to further affirmed the role of •OH and $\bullet O_2^-$ in the Mo_2C/TCN-2 photocatalytic system, electron spin resonance (ESR) instrument was conducted with DMPO as the trapping agent. Three signals were produced in Fig. 11c and 11d, which could be assigned to DMPO- $\bullet O_2^-$ and DMPO-•OH under light illumination (0 min, 4 min and 8 min). There is no ESR signal in the dark for both TCN and Mo_2C/TCN-2, but obvious signals could be detected under visible light irradiation, demonstrating the existence of $\bullet O_2^-$ and •OH in the photocatalytic system. Importantly, it can be observed that the DMPO- $\bullet O_2^-$ signal intensity for Mo_2C/TCN-2 photocatalyst were much higher than that of TCN, which was ascribe to the rapidly accumulation of free electrons to promote the generation of $\bullet O_2^-$. In addition, negligible DMPO-•OH signal can be observed over TCN under visible light irradiation, while obvious signal for Mo_2C/TCN-2 can be detected in DMPO system. The ESR result indicated the promotion effect of Mo_2C nanoparticles on the

formation of radical species ($\bullet O_2^-$ and •OH), thus leading to the significant enhancement of photocatalytic active. The obtained •OH may derived from H_2O_2 decomposing. To detect the H_2O_2 formation, the concentration of H_2O_2 was investigated, as shown in Fig. S8.

On the basis of the aforementioned experimental results, the enhanced photocatalytic performance of Mo_2C/TCN composites maybe origin from the introducing of Mo_2C, thus leading to the fast transfer of photo-induced charges and effectively restrict the recombination of electron/hole pairs in TCN. A postulated photocatalytic mechanism is proposed to illustrate the charge transfer process over Mo_2C and TCN specimens. On the one hand, the electron density migration at the Mo_2C/TCN interface was revealed by high-resolution XPS spectra. Compare to pristine Mo_2C, the Mo 3d binding energy of Mo_2C/TCN exhibited negative-shift trend, and the C 1s, N 1s binding energy of Mo_2C/TCN both exhibited positive-shift trend comparing with that of TCN [63], implying the increased electron density within Mo and C after coupling with TCN. These results confirmed that the electrons were transferred from TCN to Mo_2C. [62, 64-66]. In addition, it has been confirmed that the electrons transfer from g-C_3N_4 to Mo_2C in the Mo_2C/g-C_3N_4 photocatalytic system by other researchers [41, 43]. In the previous literature, the metallic nature and good electronic conduction of Mo_2C were reported [80, 105], thus Mo_2C could provide strong attraction to electrons [69, 77]. On the other hand, based on the UV-vis DRS spectra and Mott-Schottky plots, the E_{CB} and E_{VB} of TCN were -0.77 eV and 1.66 eV, with the homologous E_{CB} and E_{VB} of Mo_2C were -1.07 eV and 0.51 eV. The band gap structure of TCN and Mo_2C are

were mutually interlaced, complying with the type-II and direct Z-scheme charge transfer model. The E_{CB} of Mo_2C was negative than the E_{CB} of TCN, so the electrons could not transfer from the CB of TCN to the CB of Mo_2C. Combined with the XPS analysis, the electrons were transferred from the CB of TCN to the VB of Mo_2C. That is to say, the conventional type-II charge transfer model was impractical in this Mo_2C/TCN system. In addition, the VB position of Mo_2C was close to the CB position of TCN, which made the direct Z-scheme electron transfer system possible. The narrow gap of TCN and the well-matched band structure of Mo_2C offered optimized condition for constructing direct Z-scheme heterojunction. Based on the above experimental data and theoretical analysis, the mechanism of the Z-scheme system for charge transfer was proposed, as illustrated in Scheme 2. Clearly, TCN served as host scaffold to co-assemble with Mo_2C semiconductor. The photo-excited electrons in the CB of TCN could migrate to the VB of Mo_2C, where they combined holes from Mo_2C. In the Mo_2C/TCN hybrid system, Mo_2C served as electron trap that provided strong push power to fast draw the electrons generated in TCN, thus realizing effective charge separation and transportation. The high electronic conductivity of Mo_2C minimized the resistance of charge transfer, as evidenced by EIS. Mo_2C acted as highly efficient transport superhighway to quickly transfer electrons, avoiding the recombination of electron/holes and prolonging the life of photo-induce charges. In addition, the direct Z-scheme heterojunction system maintained high reducibility and oxidizing ability, thus leading to excellent photocatalytic activity. The accumulated electrons in the CB of Mo_2C could reduce O_2 into $\bullet O_2^-$ due to the CB position of Mo_2C was more negative

than the $O_2/\cdot\bullet O_2^-$ (-0.33 eV vs. NHE [106]). However, the VB of TCN was also negative than the standard redox potential of $H_2O/\bullet OH$ (2.37 eV vs. NHE [107]), the photogenerated holes cannot oxidized H_2O to •OH. The detected •OH may origin from the conversion of $\bullet O_2^-$. With respect to TC degradation, the main active specie ($\bullet O_2^-$ and h^+) and assistant specie (•OH) produced on the surface of Mo_2C/TCN could effectively degrade TC into CO_2 and H_2O, etc. The reaction process can be described as follows:

$$Mo_2C/TCN + h\upsilon \rightarrow Mo_2C/TCN\ (e^- + h^+) \quad (6)$$

$$O_2 + e^- \rightarrow \bullet O_2^- \quad (7)$$

$$\bullet O_2^- + e^- + 2H^+ \rightarrow H_2O_2 \quad (8)$$

$$H_2O_2 + e^- \rightarrow \bullet OH \quad (9)$$

$$(\bullet O_2^-, h^+, \bullet OH) + TC \rightarrow \text{products } (CO_2, H_2O, \text{etc.}) \quad (10)$$

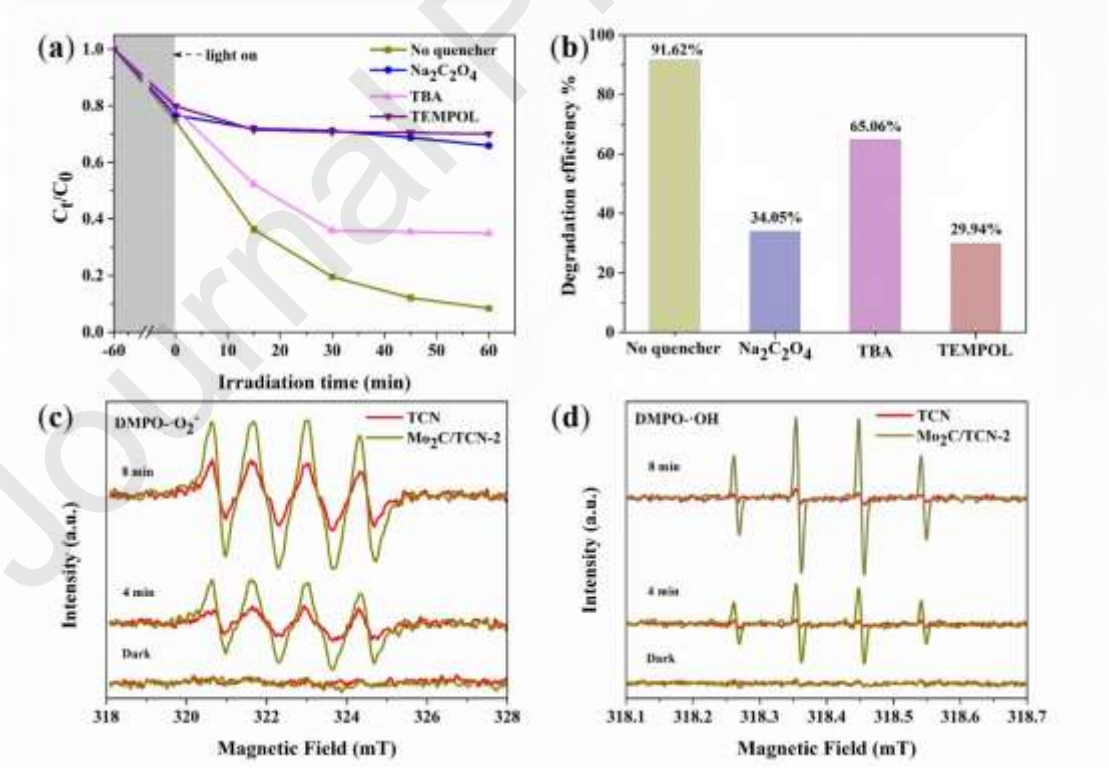

Fig. 11. (a) Photocatalytic degradation curves and (b) degradation efficiencies of TC under visible light irradiation (λ > 420 nm) over Mo_2C/TCN-2 photocatalyst with

different quenchers; ESR spectra of (c) DMPO- •O_2^- adduct and (d) DMPO- •OH adduct for TCN and Mo_2C/TCN-2 under visible light irradiation (λ > 420 nm).

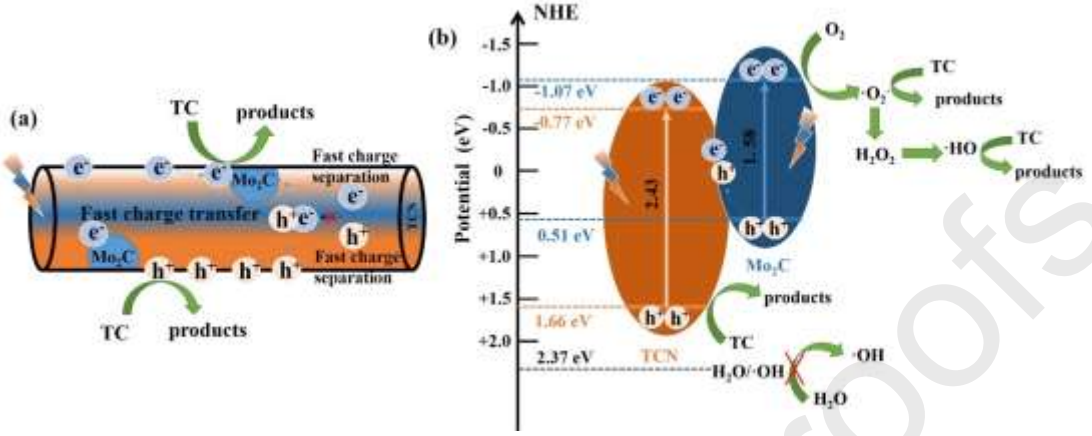

Scheme 2. Scheme for the energy band positions and spatial charge transportation and separation during photocatalytic reaction process over Mo_2C/TCN nanotubes.

4. Conclusion

In summary, a novel direct Z-scheme Mo_2C/TCN system was designed. Owing to the excellent photoelectrochemistry properties of Mo_2C, the hybrids exhibited outstanding photocatalytic performance. The TC degradation efficiency of Mo_2C/TCN-2 within 1 h irradiation reached to 91.6 %, which was about 1.6 times and 3.5 times higher than the TCN and CN. The Mo_2C demonstrated strong photo-absorption and high electronic conductivity, which enhancing the photo-absorption of Mo_2C/TCN composites in the whole spectrum and minimizing the transportation resistance for electrons transfer. The Mo_2C/TCN direct Z-scheme heterojunction has been confirmed to be favorable for the separation and transfer of photo-induce charge carriers. PL and TRPL analysis as well as electrochemical analysis proved the intensified efficiency for

the separation and transfer of electrons. The introduction of Mo_2C enhanced the visible light absorption capability as well as prolonged charge carriers' lifetime, which elevated the concentration of electrons/holes reaching the active sites of Mo_2C/TCN. This study sheds new insight for the rational design and utilization Mo_2C and g-C_3N_4 to obtained excellent photocatalytic activity. This type of direct Z-scheme heterojunction structure possesses great potential in constructing high-performance photocatalysts.

Acknowledgements

This study was financially supported by the Program for the National Natural Science Foundation of China (51809090, 51879101, 51779090, 51709101), the National Program for Support of Top–Notch Young Professionals of China (2014), the Program for Changjiang Scholars and Innovative Research Team in University (IRT-13R17), and Hunan Provincial Science and Technology Plan Project (2018SK20410, 2017SK2243, 2016RS3026), the Natural Science Foundation of Hunan Province, China (Grant Nos. 2019JJ50077) and the Fundamental Research Funds for the Central Universities (531118010114, 531119200086, 531107050978).

Journal Pre-proofs

Reference

[1] C. Zhang, C. Lai, G. Zeng, D. Huang, Efficacy of carbonaceous nanocomposites for sorbing ionizable antibiotic sulfamethazine from aqueous solution, Water Res. 95 (2016) 103-112.

[2] T. Cai, L. Wang, Y. Liu, S. Zhang, W. Dong, H. Chen, X. Yi, J. Yuan, X. Xia, C. Liu, S. Luo, Ag_3PO4/Ti_3C_2 MXene interface materials as a Schottky catalyst with enhanced photocatalytic activities and anti-photocorrosion performance, Appl. Catal. B: Environ. 239 (2018) 545-554.

[3] C. Zhang, Y. Li, D. Shuai, Y. Shen, W. Xiong, L. Wang, Graphitic carbon nitride (g-C_3N_4)-based photocatalysts for water disinfection and microbial control: A review, Chemosphere. 214 (2019) 462-479.

[4] C. Zhang, G. Zeng, D. Huang, C. Lai, M. Chen, Biochar for environmental management: Mitigating greenhouse gas emissions, contaminant treatment, and potential negative impacts, Chem. Eng. J. 373 (2019) 902-922.

[5] C. Zhang, M. Zhang, Y. Li, D. Shuai, Visible-light-driven photocatalytic disinfection of human adenovirus by a novel heterostructure of oxygen-doped graphitic carbon nitride and hydrothermal carbonation carbon, Appl. Catal. B: Environ. 248 (2019) 11-21.

[6] S. Tian, C. Zhang, D. Huang, R. Wang, G. Zeng, M. Yan, W. Xiong, C. Zhou, M. Cheng, W. Xue, Recent progress in sustainable technologies for adsorptive and reactive removal of sulfonamides, Chem. Eng. J. (2019) 123423.

[7] A. Fujishima, K. Honda, Electrochemical photolysis of water at a semiconductor electrode, Nature. 238 (1972) 37-38.

[8] R. Asahi, T. Morikawa, T. Ohwaki, K. Aoki, Y. Taga, Visible-light photocatalysis in nitrogen-doped titanium oxides, Science 293 (2001) 269-271.

[9] Y. Liu, D. Huang, M. Cheng, Z. Liu, C. Lai, Metal sulfide/MOF-based composites as visible-light-driven photocatalysts for enhanced hydrogen production from water splitting, Coordin. Chemistry. Rev. 409 (2020) 213220.

[10] Y. Shi, B. Zhang, Recent advances in transition metal phosphide nanomaterials: synthesis and applications in hydrogen evolution reaction, Chem. Soc. Rev. 45 (2016) 1529-1541.

[11] Q. Li, X. Li, CdS/graphene nanocomposite photocatalysts, Adv. Energy Mater. 5 (2015) 1500010.

[12] M. Ahmed, G. Xinxin, A review of metal oxynitrides for photocatalysis, Inorg. Chem. Front. 3 (2016) 578-590.

[13] W.-J. Ong, L.-L. Tan, Graphitic carbon nitride (g-C_3N_4)-based photocatalysts for artificial photosynthesis and environmental remediation: are we a step closer to achieving sustainability?, Chem. Rev. 116 (2016) 7159-7329.

[14] H. Luo, Z. Zeng, G. Zeng, Recent progress on metal-organic frameworks based- and derived-photocatalysts for water splitting, Chem. Eng. J. 383 (2020) 123196.

[15] A. Troupis, T. Triantis, E. Gkika, A. Hiskia, E. Papaconstantinou, Photocatalytic reductive–oxidative degradation of Acid Orange 7 by polyoxometalates, Appl. Catal. B: Environ. 86 (2009) 98-107.

[16] H. Tong, S. Ouyang, Y. Bi, N. Umezawa, M. Oshikiri, J. Ye, Nano‐photocatalytic materials: possibilities and challenges, Adv. Mater. 24 (2012) 229-251.

[17] S. Zhang, B. Li, X. Wang, G. Zhao, B. Hu, Z. Lu, T. Wen, J. Chen, X. Wang, Recent developments of two-dimensional graphene-based composites in visible-light photocatalysis for

eliminating persistent organic pollutants from wastewater, Chem. Eng. J. 390 (2020) 124642.
[18] Z. Zhang, Y. Zhu, X. Chen, H. Zhang, J. Wang, A Full-Spectrum Metal-Free Porphyrin Supramolecular Photocatalyst for Dual Functions of Highly Efficient Hydrogen and Oxygen Evolution, Adv. Mater. 31 (2019) 1806626.
[19] B. Li, C. Lai, G. Zeng, D. Huang, Black Phosphorus, a Rising Star 2D Nanomaterial in the Post-Graphene Era: Synthesis, Properties, Modifications, and Photocatalysis Applications, Small. 15 (2019) 1804565.
[20] D. He, C. Zhang, G. Zeng, Y. Yang, D. Huang, L. Wang, H. Wang, A multifunctional platform by controlling of carbon nitride in the core-shell structure: From design to construction, and catalysis applications, Appl. Catal. B: Environ. 258 (2019) 117957.
[21] X. Wang, X. Zhao, D. Zhang, G. Li, H. Li, Microwave irradiation induced UIO-66-NH_2 anchored on graphene with high activity for photocatalytic reduction of CO_2, Appl. Catal. B: Environ. 228 (2018) 47-53.
[22] C. Zhou, D. Huang, P. Xu, G. Zeng, J. Huang, T. Shi, C. Lai, C. Zhang, M. Cheng, Y. Lu, A. Duan, W. Xiong, M. Zhou, Efficient visible light driven degradation of sulfamethazine and tetracycline by salicylic acid modified polymeric carbon nitride via charge transfer, Chem. Eng. J. 370 (2019) 1077-1086.
[23] Y. Yang, G. Zeng, D. Huang, C. Zhang, D. He, Molecular engineering of polymeric carbon nitride for highly efficient photocatalytic oxytetracycline degradation and H_2O_2 production, Appl. Catal. B: Environ. (2020) 118970.
[24] Y. Wang, W. Yang, X. Chen, J. Wang, Y. Zhu, Photocatalytic activity enhancement of core-shell structure g-C_3N_4@TiO_2 via controlled ultrathin g-C_3N_4 layer, Appl. Catal. B: Environ. 220 (2018) 337-347.
[25] J. Wen, J. Xie, X. Chen, X. Li, A review on g-C_3N_4-based photocatalysts, Appl. Sur. Sci. 391 (2017) 72-123.
[26] H.-x. Zhong, Q. Zhang, J. Wang, Engineering Ultrathin C_3N_4 Quantum Dots on Graphene as a Metal-Free Water Reduction Electrocatalyst, ACS Catal. 8 (2018) 3965-3970.
[27] S. Liu, F. Chen, S. Li, X. Peng, Y. Xiong, Enhanced photocatalytic conversion of greenhouse gas CO_2 into solar fuels over g-C_3N_4 nanotubes with decorated transparent ZIF-8 nanoclusters, Appl. Catal. B: Environ. 211 (2017) 1-10.
[28] X. Wu, X. Wang, F. Wang, H. Yu, Soluble g-C_3N_4 nanosheets: Facile synthesis and application in photocatalytic hydrogen evolution, Appl. Catal. B: Environ. 247 (2019) 70-77.
[29] C. Zhou, C. Lai, C. Zhang, G. Zeng, D. Huang, Semiconductor/boron nitride composites: Synthesis, properties, and photocatalysis applications, Appl. Catal. B: Environ. 238 (2018) 6-18.
[30] Z. Zhang, C. Liu, Z. Dong, Y. Dai, G. Xiong, Y. Liu, Y. Wang, Y. Wang, Y. Liu, Synthesis of flower-like MoS_2/g-C_3N_4 nanosheet heterojunctions with enhanced photocatalytic reduction activity of uranium (VI), Appl. Sur. Sci. (2020) 146352.
[31] W. Wang, M. Chen, D. Huang, G. Zeng, An overview on nitride and nitrogen-doped photocatalysts for energy and environmental applications, Compos Part B-Eng. 172 (2019) 704-723.
[32] N. Tian, K. Xiao, Y. Zhang, X. Lu, L. Ye, P. Gao, T. Ma, H. Huang, Reactive sites rich porous tubular yolk-shell g-C_3N_4 via precursor recrystallization mediated microstructure engineering for photoreduction, Appl. Catal. B: Environ. 253 (2019) 196-205.
[33] C. Zhou, R. Shi, L. Shang, L.-Z. Wu, C.-H. Tung, T. Zhang, Template-free large-scale synthesis of g-C_3N_4 microtubes for enhanced visible light-driven photocatalytic H_2 production, Nano

Research. 11(2018) 3462-3468.
[34] W. Wang, Z. Zeng, G. Zeng, Sulfur doped carbon quantum dots loaded hollow tubular g-C_3N_4 as novel photocatalyst for destruction of Escherichia coli and tetracycline degradation under visible light, Chem. Eng. J. 378 (2019) 122132.
[35] M. Miao, J. Pan, T. He, Y. Yan, B.Y. Xia, X. Wang, Molybdenum Carbide-Based Electrocatalysts for Hydrogen Evolution Reaction, Chem. Eur. J. 23 (2017) 10947-10961.
[36] T. Ouyang, Y.Q. Ye, C.Y. Wu, K. Xiao, Z.Q. Liu, Heterostructures Composed of N-Doped Carbon Nanotubes Encapsulating Cobalt and β-Mo_2C Nanoparticles as Bifunctional Electrodes for Water Splitting, Angew. Chem. Int. Edit. 58 (2019) 4923-4928.
[37] D. Ruan, M. Fujitsuka, T. Majima, Exfoliated Mo_2C nanosheets hybridized on CdS with fast electron transfer for efficient photocatalytic H_2 production under visible light irradiation, Appl. Catal. B: Environ. 264 (2020) 118541.
[38] Y. Zhou, W. Wang, C. Zhang, D. Huang, C. Lai, M. Cheng, Sustainable hydrogen production by molybdenum carbide-based efficient photocatalysts: From properties to mechanism, Adv. Colloid Interface Sci. 279 (2020) 102144.
[39] L. Wang, Q. Zhang, J. Zhu, X. Duan, Z. Xu, Y. Liu, H. Yang, B. Lu, Nature of extra capacity in MoS_2 electrodes: molybdenum atoms accommodate with lithium, Energy Storage Mater. 16 (2019) 37-45.
[40] L. Wang, G. Zhou, H. Luo, Q. Zhang, J. Wang, C. Zhao, A.M. Rao, B. Xu, B. Lu, Enhancing catalytic activity of tungsten disulfide through topology, Appl. Catal. B: Environ. (2019) 117802.
[41] Y. Song, K. Xia, Y. Gong, H. Chen, Controllable synthesized heterostructure photocatalyst Mo_2C@C/2D g-C_3N_4: enhanced catalytic performance for hydrogen production, Dalton T. 47 (2018) 14706-14712.
[42] J. Zhang, M. Wu, B. He, Facile synthesis of rod-like g-C_3N_4 by decorating Mo_2C co-catalyst for enhanced visible-light photocatalytic activity, Appl. Surf. Sci. 470 (2019) 565-572.
[43] Y. Zou, D. Ma, D. Sun, S. Mao, C. He, Carbon nanosheet facilitated charge separation and transfer between molybdenum carbide and graphitic carbon nitride toward efficient photocatalytic H2 production, Appl. Surf. Sci. 473 (2019) 91-101.
[44] C. Lei, W. Zhou, L. Shen, X. Zheng, Q. Feng, Y. Liu, Y. Lei, S. Liang, D. Zhang, L. Jiang, Enhanced Selective H_2S Oxidation Performance on Mo_2C-Modified g-C_3N_4, ACS Sustain. Chem. Eng. 7 (2019) 16257-16263.
[45] Z. Wang, H. Wang, Z. Zeng, G. Zeng, Metal-organic frameworks derived $Bi_2O_2CO_3$/porous carbon nitride: A nanosized Z-scheme systems with enhanced photocatalytic activity, Appl. Catal. B: Environ. 267 (2020) 118700.
[46] Z. Tong, D. Yang, Y. Sun, Y. Nan, Z. Jiang, Tubular g-C_3N_4 isotype heterojunction: Enhanced visible-light photocatalytic activity through cooperative manipulation of oriented electron and hole transfer, Small. 12 (2016) 4093-4101.
[47] J. Dong, Q. Wu, C. Huang, Cost effective Mo rich Mo_2C electrocatalysts for the hydrogen evolution reaction, J. Mater. Chem. A. 6 (2018) 10028-10035.
[48] R. Yin, Q. Luo, D. Wang, SnO_2/g-C_3N_4 photocatalyst with enhanced visible-light photocatalytic activity, J. Mater. Sci. 49 (2014) 6067-6073.
[49] C. Zhou, Z. Zeng, G. Zeng, D. Huang, Visible-light-driven photocatalytic degradation of sulfamethazine by surface engineering of carbon nitrideProperties, degradation pathway and mechanisms, J Hazard Mater. 380 (2019) 120815.

[50] T. Xiong, W. Cen, Y. Zhang, Bridging the g-C_3N_4 Interlayers for Enhanced Photocatalysis, ACS Catalysis. 6 (2016) 2462-2472.

[51] Z. Sun, J.M.T.A. Fischer, Q. Li, J. Hu, Enhanced CO_2 photocatalytic reduction on alkali-decorated graphitic carbon nitride, Appl. Catal. B: Environ. 216 (2017) 146-155.

[52] H. Huang, K. Xiao, N. Tian, F. Dong, Template-free precursor-surface-etching route to porous, thin g-C_3N_4 nanosheets for enhancing photocatalytic reduction and oxidation activity, J. Mater. Chem. A. 5 (2017) 17452-17463.

[53] P. Niu, M. Qiao, Y. Li, L. Huang, T. Zhai, Distinctive defects engineering in graphitic carbon nitride for greatly extended visible light photocatalytic hydrogen evolution, Nano Energy. 44 (2018) 73-81.

[54] J.C. Wang, H.C. Yao, Z.Y. Fan, Indirect Z-Scheme BiOI/g-C_3N_4 Photocatalysts with Enhanced Photoreduction CO_2 Activity under Visible Light Irradiation, ACS Appl. Mater. Inter. 8 (2016) 3765-3775.

[55] C. Li, Y. Du, D. Wang, S. Yin, W. Tu, Z. Chen, M. Kraft, G. Chen, R. Xu, Unique P-Co-N surface bonding states constructed on g-C_3N_4 nanosheets for drastically enhanced photocatalytic activity of H_2 evolution, Adv. Funct. Mate. 27 (2017) 1604328.

[56] S. Jing, L. Zhang, L. Luo, J. Lu, S. Yin, P.K. Shen, P. Tsiakaras, N-Doped Porous Molybdenum Carbide Nanobelts as Efficient Catalysts for Hydrogen Evolution Reaction, Appl. Catal. B: Environ. 224 (2018) 533-540.

[57] M.A.R. Anjum, M.H. Lee, J.S. Lee, BCN network-encapsulated multiple phases of molybdenum carbide for efficient hydrogen evolution reactions in acidic and alkaline media, J. Mater. Chem. A. 5 (2017) 13122-13129.

[58] Y. Huang, Q. Gong, X. Song, Mo_2C nanoparticles dispersed on hierarchical carbon microflowers for efficient electrocatalytic hydrogen evolution, ACS nano. 10 (2016) 11337-11343.

[59] L.F. Pan, Y.H. Li, S. Yang, P.F. Liu, Molybdenum carbide stabilized on graphene with high electrocatalytic activity for hydrogen evolution reaction, Chem. Commun. 50 (2014) 13135-13137.

[60] C. Wan, Y.N. Regmi, B.M. Leonard, Multiple phases of molybdenum carbide as electrocatalysts for the hydrogen evolution reaction, Angew Chem. 53 (2014) 6407-6410.

[61] R. Ma, Y. Zhou, Y. Chen, P. Li, Q. Liu, J. Wang, Ultrafine molybdenum carbide nanoparticles composited with carbon as a highly active hydrogen-evolution electrocatalyst, Angew. Chem. 54 (2015) 14723-14727.

[62] R. Tang, S. Zhou, L. Zhang, L. Yin, Metal-organic framework derived narrow bandgap cobalt carbide sensitized titanium dioxide nanocage for superior photo-electrochemical water oxidation performance, Adv. Funct. Mater. 28 (2018) 1706154.

[63] J. Dong, Y. Shi, C. Huang, Q. Wu, T. Zeng, W. Yao, A New and stable Mo-Mo_2C modified g-C_3N_4 photocatalyst for efficient visible light photocatalytic H_2 production, Appl. Catal. B: Environ. 243 (2019) 27-35.

[64] H. Gao, H. Yang, J. Xu, S. Zhang, J. Li, Strongly coupled g-C_3N_4 nanosheets-Co_3O_4 quantum dots as 2D/0D heterostructure composite for peroxymonosulfate activation, Small. (2018) 1801353.

[65] S. Zhang, H. Gao, X. Liu, Y. Huang, Hybrid 0D–2D nanoheterostructures: In situ growth of amorphous silver silicates dots on g-C_3N_4 nanosheets for full-spectrum photocatalysis, ACS Appli. Materi. Inter. 8 (2016) 35138-35149.

[66] D. Jiang, J. Li, C. Xing, Z. Zhang, S. Meng, M. Chen, Two-dimensional $CaIn_2S_4$/g-C_3N_4 heterojunction nanocomposite with enhanced visible-light photocatalytic activities: Interfacial

engineering and mechanism insight, ACS Appl. Mater. Inter. 7 (2015) 19234-19242.
[67] P. Xia, B. Zhu, J. Yu, S. Cao, M. Jaroniec, Ultra-thin nanosheet assemblies of graphitic carbon nitride for enhanced photocatalytic CO_2 reduction, J. Mater. Chem. A. 5 (2017) 3230-3238.
[68] P. Chen, F. Liu, H. Ding, S. Chen, Porous double-shell CdS@C_3N_4 octahedron derived by in situ supramolecular self-assembly for enhanced photocatalytic activity, Appl. Catal. B: Environ. 252 (2019) 33-40.
[69] X. Yue, S. Yi, R. Wang, Z. Zhang, S. Qiu, Well-controlled $SrTiO_3$@Mo_2C core-shell nanofiber photocatalyst: boosted photo-generated charge carriers transportation and enhanced catalytic performance for water reduction, Nano energy. 47 (2018) 463-473.
[70] M. Nowak, B. Kauch, P. Szperlich, Determination of energy band gap of nanocrystalline SbSI using diffuse reflectance spectroscopy, Rev. Sci. Instrum. 80 (2009) 046107.
[71] H.Q. Xu, J. Hu, D. Wang, Z. Li, Visible-Light Photoreduction of CO_2 in a Metal-Organic Framework: Boosting Electron-Hole Separation via Electron Trap States, J. Am. Chem. Soc. 137 (2015) 13440-13443.
[72] T.W. Kim, K.-S. Choi, Nanoporous $BiVO_4$ photoanodes with dual-layer oxygen evolution catalysts for solar water splitting, Science. 343 (2014) 990-994.
[73] X. Li, J. Yu, J. Low, Y. Fang, J. Xiao, X. Chen, Engineering heterogeneous semiconductors for solar water splitting, J. Mater. Chem. A. 3 (2015) 2485-2534.
[74] J. Zhang, L. Qi, J. Ran, J. Yu, S.Z. Qiao, Ternary NiS/$Zn_xCd_{1-x}S$/Reduced Graphene Oxide Nanocomposites for Enhanced Solar Photocatalytic H_2-Production Activity, Adv. Energy Mater. 4 (2014) 1301925.
[75] X. Wang, C. Liow, A. Bisht, X. Liu, Engineering interfacial photo-induced charge transfer based on nanobamboo array architecture for efficient solar-to-chemical energy conversion, Adv. Mater. 27 (2015) 2207-2214.
[76] Y. Yang, Z. Zeng, G. Zeng, D. Huang, Ti_3C_2 Mxene/porous g-C_3N_4 interfacial Schottky junction for boosting spatial charge separation in photocatalytic H_2O_2 production, Appl. Catal. B: Environ. 258 (2019) 117956.
[77] X. Yue, S. Yi, R. Wang, Z. Zhang, S. Qiu, A novel architecture of dandelion-like Mo_2C/TiO_2 heterojunction photocatalysts towards high-performance photocatalytic hydrogen production from water splitting, J. Mater. Chem. A. 5 (2017) 10591-10598.
[78] H. Chauhan, Y. Kumar, J. Dana, B. Satpati, Photoinduced ultrafast charge separation in colloidal 2-dimensional CdSe/CdS-Au hybrid nanoplatelets and corresponding application in photocatalysis, Nanoscale. 8 (2016) 15802-15812.
[79] Q. Gao, X. Zhao, Y. Xiao, A mild route to mesoporous Mo_2C-C hybrid nanospheres for high performance lithium-ion batteries, Nanoscale. 6 (2014) 6151-6157.
[80] L. Yang, X. Li, Y. Ouyang, Hierarchical MoO_2/Mo_2C/C hybrid nanowires as high-rate and long-life anodes for lithium-ion batteries, ACS Appl. Mater. Inter. 8 (2016) 19987-19993.
[81] N.T.T. Ha, O.V. Lefedova, N.N. Ha, Theoretical study on the adsorption of carbon dioxide on individual and alkali-metal doped MOF-5s, Russ. J. Phys. Chem. A. 90 (2015) 220-225.
[82] S. Ye, M. Yan, X. Tan, J. Liang, G. Zeng, Facile assembled biochar-based nanocomposite with improved graphitization for efficient photocatalytic activity driven by visible light, Appl. Catal. B: Environ. 250 (2019) 78-88.
[83] C. Zhang, W. Wang, A. Duan, G. Zeng, D. Huang, C. Lai, X. Tan, M. Cheng, R. Wang, C. Zhou, W. Xiong, Y. Yang, Adsorption behavior of engineered carbons and carbon nanomaterials for metal

endocrine disruptors: Experiments and theoretical calculation, Chemosphere. 222 (2019) 184-194.
[84] S. Rangabhashiyam, N. Anu, M.S. Giri Nandagopal, N. Selvaraju, Relevance of isotherm models in biosorption of pollutants by agricultural byproducts, J. Environ. Chem. Eng. 2 (2014) 398-414.
[85] H. Li, W. Hong, Y. Cui, S. Fan, L. Zhu, Effect of Mo_2C content on the structure and photocatalytic property of Mo_2C/TiO_2 catalysts, J. Alloy Compd. 569 (2013) 45-51.
[86] Y.-C. Nie, F. Yu, L.-C. Wang, Q.-J. Xing, X. Liu, Y. Pei, Photocatalytic degradation of organic pollutants coupled with simultaneous photocatalytic H 2 evolution over graphene quantum dots/Mn-N-TiO_2/g-C_3N_4 composite catalysts: Performance and mechanism, Appl. Catal. B: Environ. 227 (2018) 312-321.
[87] X.F. Tan, Y.G. Liu, Y.L. Gu, S.B. Liu, Biochar pyrolyzed from MgAl-layered double hydroxides pre-coated ramie biomass (Boehmeria nivea (L.) Gaud.): Characterization and application for crystal violet removal, J. Environ. Manage. 184 (2016) 85-93.
[88] Z. Zeng, S. Ye, H. Wu, R. Xiao, G. Zeng, Research on the sustainable efficacy of g-MoS_2 decorated biochar nanocomposites for removing tetracycline hydrochloride from antibiotic-polluted aqueous solution, Sci. Total Environ. 648 (2019) 206-217.
[89] B. Li, C. Lai, G. Zeng, L. Qin, H. Yi, D. Huang, Facile Hydrothermal Synthesis of Z-Scheme $Bi_2Fe_4O_9/Bi_2WO_6$ Heterojunction Photocatalyst with Enhanced Visible Light Photocatalytic Activity, ACS Appl. Mater. Inter. 10 (2018) 18824-18836.
[90] B. Zhou, X. Zhao, H. Liu, J. Qu, C.P. Huang, Visible-light sensitive cobalt-doped $BiVO_4$ (Co-$BiVO_4$) photocatalytic composites for the degradation of methylene blue dye in dilute aqueous solutions, Appl. Catal. B: Environ. 99 (2010) 214-221.
[91] C. Zhang, C. Lai, G. Zeng, D. Huang, L. Tang, C. Yang, Y. Zhou, L. Qin, M. Cheng, Nanoporous Au-based chronocoulometric aptasensor for amplified detection of Pb(2+) using DNAzyme modified with Au nanoparticles, Biosens Bioelectron. 81 (2016) 61-67.
[92] L. Tang, J. Wang, G. Zeng, Y. Liu, Y. Deng, Enhanced photocatalytic degradation of norfloxacin in aqueous Bi_2WO_6 dispersions containing nonionic surfactant under visible light irradiation, J. Hazard Mater. 306 (2016) 295-304.
[93] J. Cao, Z.-h. Yang, W.-p. Xiong, One-step synthesis of Co-doped UiO-66 nanoparticle with enhanced removal efficiency of tetracycline: Simultaneous adsorption and photocatalysis, Chem. Eng. J. 353 (2018) 126-137.
[94] F. Deng, L. Zhao, X. Luo, S. Luo, Highly efficient visible-light photocatalytic performance of $Ag/AgIn_5S_8$ for degradation of tetracycline hydrochloride and treatment of real pharmaceutical industry wastewater, Chem. Eng. J. 333 (2018) 423-433.
[95] W. Wang, P. Xu, M. Chen, G. Zeng, Alkali Metal-Assisted Synthesis of Graphite Carbon Nitride with Tunable Band-Gap for Enhanced Visible-Light-Driven Photocatalytic Performance, ACS Sus. Chem. Eng. 6 (2018) 15503-15516.
[96] Y.-Y. Chen, Y.-L. Ma, J. Yang, Aqueous tetracycline degradation by H_2O_2 alone: Removal and transformation pathway, Chem. Eng. J. 307 (2017) 15-23.
[97] M.H. Khan, H. Bae, J.Y. Jung, Tetracycline degradation by ozonation in the aqueous phase: proposed degradation intermediates and pathway, J. Hazard Mater. 181 (2010) 659-665.
[98] J. Wang, D. Zhi, H. Zhou, X. He, D. Zhang, Evaluating tetracycline degradation pathway and intermediate toxicity during the electrochemical oxidation over a Ti/Ti_4O_7 anode, Water Res. 137(2018) 324-334.

[99] M. Yan, Y. Wu, F. Zhu, Y. Hua, W. Shi, The fabrication of a novel Ag_3VO_4/WO_3 heterojunction with enhanced visible light efficiency in the photocatalytic degradation of TC, Phys. Chem. Chem. Phys. 18 (2016) 3308-3315.

[100] H. Dong, Z. Jiang, C. Zhang, Removal of tetracycline by Fe/Ni bimetallic nanoparticles in aqueous solution, J. Colloid Interface Sci. 513 (2018) 117-125.

[101] Z. Xie, Y. Feng, F. Wang, D. Chen, Construction of carbon dots modified $MoO_3/g\text{-}C_3N_4$ Z-scheme photocatalyst with enhanced visible-light photocatalytic activity for the degradation of tetracycline, Appl. Catal. B: Environ. 229 (2018) 96-104.

[102] Y. Xu, D. Lin, X. Liu, Y. Luo, Electrospun $BiOCl/Bi_2Ti_2O_7$ nanorod heterostructures with enhanced solar light efficiency in the photocatalytic degradation of Tetracycline hydrochloride, ChemCatChem. 10 (2018) 2496-2504.

[103] Y. Yang, C. Zhang, D. Huang, Boron nitride quantum dots decorated ultrathin porous $g\text{-}C_3N_4$: Intensified exciton dissociation and charge transfer for promoting visible-light-driven molecular oxygen activation, Appl. Catal. B: Environ. 245 (2019) 87-99.

[104] C. Zhou, C. Lai, D. Huang, G. Zeng, Highly porous carbon nitride by supramolecular preassembly of monomers for photocatalytic removal of sulfamethazine under visible light driven, Appl. Catal. B: Environ. 220 (2018) 202-210.

[105] M. Shi, L. Zhao, X. Song, J. Liu, P. Zhang, L. Gao, Highly conductive Mo_2C nanofibers encapsulated in ultrathin MnO_2 nanosheets as a self-supported electrode for high-performance capacitive energy storage, ACS Appl. Mater. Inter. 8 (2016) 32460-32467.

[106] L. Jiang, X. Yuan, G. Zeng, J. Liang, In-situ synthesis of direct solid-state dual Z-scheme $WO_3/g\text{-}C_3N_4$ /Bi_2O_3 photocatalyst for the degradation of refractory pollutant, Appl. Catal. B: Environ. 227 (2018) 376-385.

[107] Y. Xie, S. Yu, Y. Zhong, Q. Zhang, Y. Zhou, SnO_2/graphene quantum dots composited photocatalyst for efficient nitric oxide oxidation under visible light, Appl. Surf. Sci. 448 (2018) 655-661.

Journal Pre-proofs

Graphical Abstract

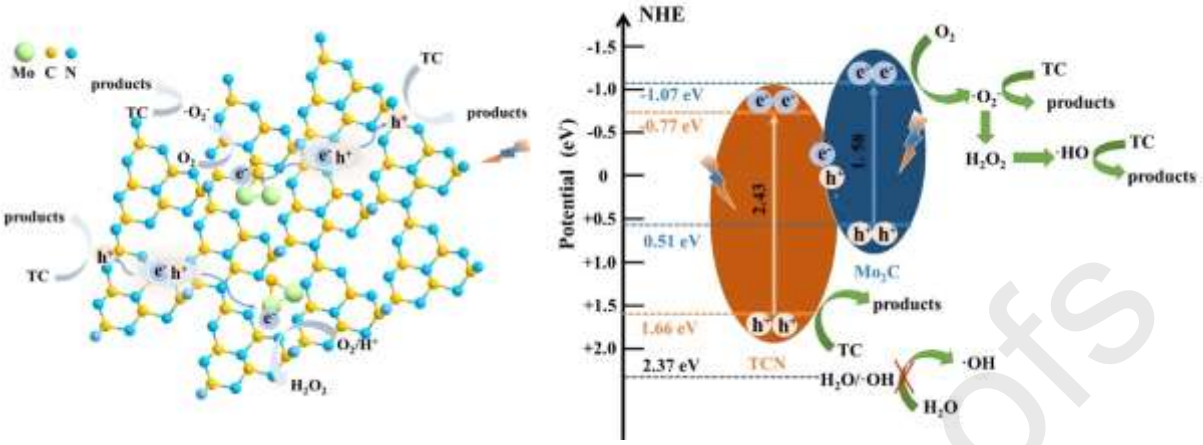

Journal Pre-proofs

- Mo_2C/TCN direct Z−Scheme heterostructure photocatalysts were synthesized
- The improvement in the activity is ascribed to the synergistic effects of Mo_2C and TCN.
- 2 wt% Mo_2C/TCN exhibits high photocatalytic activity and is stable in real water.
- Effective charge transfer and separation was realized across the Z−Scheme system.
- Mo_2C acts as an electron trap and plays an important role in the charge transfer.

Journal Pre-proofs

Declaration of interests

The authors declare that they have no known competing financial interests or personal relationships that could have appeared to influence the work reported in this paper.

Journal Pre-proofs

Credit Author Statement

Title： Formation of Mo_2C/hollow tubular g-C_3N_4 hybrids with favorable charge transfer channels for excellent visible-light-photocatalytic performance

Authors: Chen Zhang *, Yin Zhou, Wenjun Wang, Yang Yang, Chengyun Zhou, Longlu Wang , Lei Lei , Donghui He, Hanzhuo Luo, Danlian Huang *

Credit Author Statement

Yin Zhou, Danlian Huang,Chen Zhang: designed the project;

Yin Zhou: wrote the Manuscript;

Yin Zhou, Wenjun Wang, Yang Yang, Chengyun Zhou, Longlu Wang: processed datas;

Lei Lei, Donghui He, Hanzhuo Luo: polished this paper.

Signed by all authors as follows: Chen Zhang *, Yin Zhou, Wenjun Wang, Yang Yang, Chengyun Zhou, Longlu Wang , Lei Lei , Donghui He, Hanzhuo Luo, Danlian Huang*

Journal Pre-proofs